SIAM J. IMAGING SCIENCES Vol. 16, No. 3, pp. 1398–1439

© 2023 Society for Industrial and Applied Mathematics

Orthogonal Matrix Retrieval with Spatial Consensus for 3D Unknown View Tomography

Shuai Huang † , Mona Zehni ‡ , Ivan Dokmanić § , and Zhizhen Zhao †

Abstract. Unknown view tomography (UVT) reconstructs a 3D density map from its 2D projections at undesign an easy-to-compute initial density map which effectively mitigates the nonconvexity of the orthogonal matrices by requiring that they be mutually consistent. in the typical low signal-to-noise-ratio scenario of 3D UVT. is more robust and performs significantly better than the previous state-of-the-art reconstruction problem. Experimental results show that the proposed OMR with spatial consensus This is enabled by the new closed-form expressions for spatial autocorrelation features. Further, we nonconvex optimization problem by a denoised reference projection and a nonnegativity constraint. OMR to break free from those restrictions, we propose to jointly recover the density map and the quire side information about the density that is not available or fail to be sufficiently robust. matrix retrieval (OMR) approaches based on matrix factorization, which, while elegant, either remoments with rotation-invariant Fourier features to solve UVT in the frequency domain, assuming that the orientations are uniformly distributed. This line of work includes the recent orthogonal known, random orientations. A line of work starting with Kam (1980) employs the method of We regularize the resulting

Key words. unknown view tomography, single-particle cryo-electron microscopy, method of moments, autocorrelation, spherical harmonics

MSC codes. 92C55, 68U10, 33C55, 78M05

DOI. 10.1137/22M1498218

reconstruction. The first approach proceeds by alternating between reconstructing the density whether the particle orientations need to be estimated, there are generally two approaches to ratio (SNR) of projection images make this reconstruction a challenging task. Depending on molecular density map [12]. The unknown particle orientations and the low signal-to-noise molecules are taken at random, unknown view angles and then used to reconstruct the 3D particle cryo-electron microscopy (cryo-EM), where noisy projections of biological macro-Introduction. Unknown view tomography (UVT) arises in applications such as single-

electronically August 8, 2023. $\hat{\ \ }$ Received by the editors July 7, 2022; accepted for publication (in revised form) March 14, 2023; published

https://doi.org/10.1137/22M1498218

Funding: The third author was supported by the European Research Council (ERC) Starting Grant 852821—SWING. The second and fourth authors were partly supported by NSF DMS-1854791, NSF OAC-1934757, and the Alfred P. Sloan Foundation.

[†]Department of Radiology and Imaging Sciences, Emory University, Atlanta, GA 30329 USA (shuai.huang@

illinois edu, zhizhenz@illinois edu) ‡ Coordinate Science Laboratory, University of Illinois at Urbana-Champaign, Urbana, IL 61801 USA (mzehni20

dokmanic@unibas.ch) [§]Department of Mathematics and Computer Science, University of Basel, 4001 Basel, Switzerland (ivan

templates at each iteration, this approach is computationally expensive. tion algorithm [13, 29, 30, 33]. Since all projection images need to be matched to reference density map is computed as the maximum a posteriori estimate via the expectation maximiza-Soft assignments are thus adopted in the form of posterior distributions over view angles. The more noise than signal (SNR < 1), it is hard to estimate the particle orientations accurately. map and estimating the particle orientations. Since the projection images typically contain

map through autocorrelation analysis on the micrographs directly. from micrographs. Bendory et al. [7] also showed that it is possible to recover the density general, the moments are calculated with respect to single-particle projection images cropped complexity of the MoM with moments of order up to m scales at a rate of $1/\text{SNR}^m$ [3]. In number of required projection images [34]. For uniformly distributed orientations, the sample cutoff order, and the noise amplification in higher-order moments drastically increases the fourth-order moments, the computational complexity scales exponentially with the momenttures. Higher-order moments come with a price: while it is possible to use the third- or even that the first- and second-order moments suffice to determine a finite list of possible strucknown view angles. For a known, nonuniform rotation distribution, Sharon et al. [32] showed order moments suffices for unique recovery if they are complemented by two projections with uses the first- and second-order moments. Levin et al. [24] have shown that using secondfirst-, second-, and third-order moments [3]. Autocorrelation analysis, however, primarily list recovery— [21, 22, 23]. For uniformly distributed orientations, it is known that the MoM achieves generic sity map through autocorrelation analysis, an instance of the method of moments (MoM) The second approach bypasses estimation of particle orientations and recovers the den--determining the density map up to a finite list of candidate densities—from

difficult to get accurate orientation estimations. to a set of unknown orthogonal matrices. They are useful in the low SNR regime, where it is the spherical harmonic expansion coefficients of the Fourier transform of the density map up jection images assuming that particle orientations are uniformly distributed. They determine number of follow-up works [9, 24, 32]. Fourier autocorrelations can be estimated from the proinvariant second-order moments [22]. The same moments were used for reconstruction in a Kam proposed an MoM approach with Fourier autocorrelation functions which are rotation-

is not robust enough to handle complicated density maps (cf. section 6). requires (at least) two denoised projection images to perform the reconstruction. However, it known. Levin et al. [24] describe an improved OMR by projection matching (OMR-PM) which from two unknown structures and assumes the differences between the two structures are a similar molecule and the orthogonal replacement method which requires projection images [9] describe two algorithms: the orthogonal extension method which requires the structure of additional information that is usually not available. For example, Bhamre, Zhang, and Singer orthogonal matrix retrieval (OMR) problem [9, 24]. Existing OMR methods, however, require expansion coefficients can be either solved for directly [23, 32] or recovered by solving an the MoM with rotation-invariant features [9, 22, 23, 24, 32, 35]. Kam's spherical harmonic Our proposed approach builds on the line of work spearheaded by Kam and leverages

work, however, employs a parametric point-source density map which does not scale easily to the density map can be directly optimized in the spatial domain [20, 41, 42]. realistic molecular density maps. On the other hand, earlier work on unassigned distance geometry and UVT shows that

- both the orthogonal matrices and the density map for a consistent recovery. 1.1. Our contributions and paper outline. We formulate the reconstruction in terms of
- We propose novel radial and autocorrelation features in the spatial domain. Compared form expressions in terms of the density map. to Fourier autocorrelations, the proposed spatial autocorrelations have simpler closed-
- orthogonal matrices. optimization, so that the spatial consensus on the density can be enforced among the the orthogonal matrices to the density map and recover them jointly via alternating difficult to incorporate spatial information through the orthogonal matrices. We relate Previous OMR approaches recover only the orthogonal matrices, and it has been
- matches the reference projection. image. This initialization provides the basis for the orthogonal matrices to "reach a program that involves the spatial radial features and a denoised reference projection To make this work, we construct an initial density by solving a convex optimization consensus" on a density that additionally satisfies the nonnegativity constraints and

data are available at https://github.com/shuai-huang/OMR-SC. and that it excels in the low-SNR regime that is common in UVT. Reproducible code and robust across a range of different density maps than the previous state-of-the-art OMR-PM Experimental results show that the proposed OMR with spatial consensus (OMR-SC) is more

results are given in the supplementary material (UVT_SIIMS_Supplementary.pdf [local/web in section 6, and we conclude the paper with a discussion in section 7. Additional experimental the OMR-SC and OMR-PM approaches on the recovery of random and protein density maps autocorrelation features, we propose the OMR-SC approach in section 5. We then compare and the density map is parameterized in section 4. Building on the parametric radial and autocorrelation features and their relations to Fourier features are then introduced in section 3, Kam's autocorrelation analysis in the frequency domain. The proposed spatial radial and Paper outline. In section 2, we first set up the mathematical model for UVT and review

Downloaded 08/27/23 to 130.126.143.60. Redistribution subject to SIAM license or copyright; see https://epubs.siam.org/terms-privacy

supplementary material. For readers' convenience, we provide a list of notations of the variables in Table SM1 in the lower-case letters to represent vectors, and boldface upper-case letters to represent matrices. Notation. We use nonboldface lower- and upper-case letters to represent scalars, boldface

2. UVT via the MoM.

supported within a ball, approximately bandlimited with an effective bandwidth π , and squarewhere $r = [x \ y \ z]^T \in \mathbb{R}^3$ contains the Cartesian coordinates. We assume $\rho(r)$ is compactly **Problem formulation.** Let $r \mapsto \rho(r)$ denote the 3D density map to be estimated,

noiseless projection $P_n(x,y)$ along the z-direction is representing a 3D rotation $\chi_n \in SO(3)$. As illustrated in Figure 1, our input data consist of N projection images, each containing projection of ρ at some unknown orientation. Let \mathbf{R}_n denote the 3×3 rotation matrix The rotated density model is then $\rho(R_n^T r)$.

¹Since supp (ρ) is compact, square integrability implies integrability

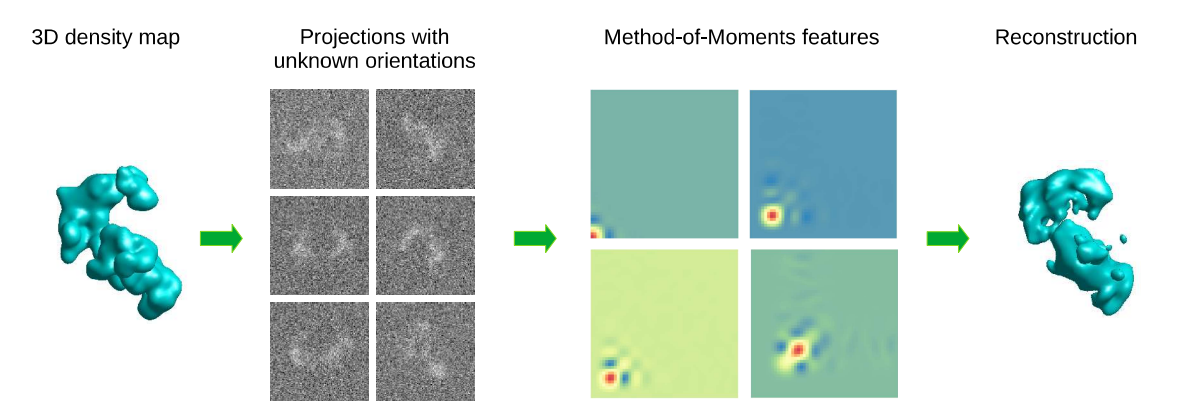


Figure 1. The UVT via the MoM.

(2.1) Noiseless projection:
$$P_n(x,y) = \int_{-\infty}^{\infty} \rho\left(\mathbf{R}_n^T[x\ y\ z]^T\right) \ dz$$
.

It is further corrupted by additive noise $\varepsilon_n(x,y)$ to produce the observed noisy projection image $S_n(x,y)$,

(2.2) Noisy projection:
$$S_n(x,y) = P_n(x,y) + \varepsilon_n(x,y)$$
.

The noise ε_n is modeled as white Gaussian noise with variance estimated from the measured data [6]. In practice, images of individual particles are cropped from the micrographs. Additional in-plane translation misalignment may occur when the particle is not centered during particle picking; a number of methods are available to mitigate it [8, 19, 39, 40, 45]. In this paper, we extract rotation-invariant features from the projection images and assume that the particles have been properly centered in the projection images. Although the distribution of particle orientations is not strictly uniform in practice, the uniform assumption is widely adopted by MoM approaches and has enjoyed empirical successes [9, 22, 24]. Here we also assume that the unknown rotations $\chi_n \in SO(3)$ are uniformly distributed in SO(3). Our goal is then to reconstruct the 3D density map $\rho(\mathbf{r})$ from a collection of 2D noisy projection images $\{S_n \mid n=1,\ldots,N\}$ with unknown, uniformly distributed view directions.

2.2. Kam's autocorrelation analysis in the frequency domain. We next review the recent developments in Kam's autocorrelation analysis and discuss the limitations of previous OMR approaches in this subsection. The MoM approach proposed by Kam performs the reconstruction in the frequency domain using autocorrelation features extracted from 2D projections [21, 22]. The Fourier transform $\hat{\rho}(\mathbf{k})$ of the 3D density map $\rho(\mathbf{r})$ is given by

(2.3)
$$\widehat{\rho}(\mathbf{k}) = \iiint e^{-i\mathbf{k}\cdot\mathbf{r}} \rho(\mathbf{r}) d\mathbf{r} = \iiint e^{-ikr\cos\alpha} \rho(\mathbf{r}) d\mathbf{r},$$

where \mathbf{i} is the imaginary unit, $\mathbf{k} = [k_x \ k_y \ k_z]^T \in \mathbb{R}^3$ is the frequency, $k = ||\mathbf{k}||$ is the norm of \mathbf{k} , $r = ||\mathbf{r}||$ is the norm of \mathbf{r} , and α is the angle between \mathbf{k} and \mathbf{r} . We shall write $\mathbf{a} = a\ddot{\mathbf{a}}$ with $a = ||\mathbf{a}||$ and $||\ddot{\mathbf{a}}|| = 1$ for the polar representation of a generic vector $\mathbf{a} \in \mathbb{R}^3$.

harmonic expansion coefficients $\{A_{lm}(k)\}_{lm}$ of $\widehat{\rho}(k)$. We have The Fourier autocorrelation features used by MoM are expressed in terms of the spherical

(2.4)
$$\widehat{\rho}(\mathbf{k}) = \sum_{l=0}^{\infty} \sum_{m=-l}^{l} A_{lm}(k) \cdot Y_{lm}(\theta_{\mathbf{k}}, \varphi_{\mathbf{k}}).$$

of degree l and order m. Note that $A_{lm}(k)$ is purely real for even l and purely imaginary for where (θ_k, φ_k) is the angular direction of k and $Y_{lm}(\cdot)$ is the real spherical harmonic function

$$(2.5) A_{lm}(k) = \iiint \widehat{\rho}(\tilde{\mathbf{k}}) \cdot \delta(k - \tilde{k}) \cdot Y_{lm}(\theta_{\tilde{\mathbf{k}}}, \varphi_{\tilde{\mathbf{k}}}) \cdot \sin \theta_{\tilde{\mathbf{k}}} \ d\tilde{k} d\theta_{\tilde{\mathbf{k}}} d\varphi_{\tilde{\mathbf{k}}};$$

where $\delta(\cdot)$ is the Dirac impulse. Features are computed from the 2D projection images. The 2D Fourier transform \hat{S}_n of a

(2.6)
$$\widehat{S}_n(k_x, k_y) = \iint \exp\left(-i \cdot [k_x \ k_y] \left[\begin{array}{c} x \\ y \end{array} \right] \right) \cdot S_n(x, y) \ dx \ dy$$

From the central slice theorem, the above \widehat{S}_n corresponds to a central slice of $\widehat{\rho}(k)$ [26, Appendices B and C],

$$\widehat{S}_{n}(k_{x}, k_{y}) = \widehat{\rho}\left(\mathbf{R}_{n}^{T}[k_{x} \ k_{y} \ 0]^{T}\right) + \widehat{\epsilon}(k_{x}, k_{y})$$

$$= \sum_{l=0}^{\infty} \sum_{m=-l}^{l} \sum_{m'=-l}^{l} A_{lm}(k) \cdot Y_{lm'}\left(\frac{\pi}{2}, \varphi_{\mathbf{k}}\right) \cdot D_{mm'}^{l}(\chi_{n}) + \widehat{\epsilon}(k_{x}, k_{y}),$$

the Fourier slice S_n is the same as the relative position of their "true" 3D counterparts since $[k_x, k_y, 0][k_x', k_y', 0]^T = [k_x, k_y, 0] \mathbf{R} \mathbf{R}^T [k_x', k_y', 0]^T$ for any rotation \mathbf{R} . (In particular, this allows where $\varphi_{\mathbf{k}} = \operatorname{atan2}(k_y, k_x)$, and $D^l_{mm'}(\chi_n)$ is an element of the Wigner D-matrix. However, since the rotation χ_n (that is to say, \mathbf{R}_n) is unknown, we do not know a priori which central slice \widehat{S}_n corresponds to. What we do know is that the relative position of two frequencies in us to compute the correct length of a frequency vector in the slice.)

or, equivalently, over all the Fourier slices [21], SO(3), Kam proposed to estimate the autocorrelation function $C_N(k_1, k_2, \psi)$ of the Fourier transform $\hat{\rho}(\mathbf{k})$ in the frequency domain by averaging $\hat{S}_n(\mathbf{k}_1)\hat{S}_n^*(\mathbf{k}_2)$ over all the projections, be the azimuth angle of k_1 , and ψ be the angle between k_1 and k_2 such that φ_{k_1} Let k_1 and k_2 denote two frequency vectors in the same 2D Fourier slice \hat{S}_n , $\varphi_{k_1} = \angle k_1$ Assuming that the rotations $\{\chi_n\}_{n=1}^N$ are drawn uniformly from the rotation group

$$(2.8) C_N(k_1, k_2, \psi) = \frac{1}{N} \sum_{n=1}^{N} \frac{1}{2\pi} \int_0^{2\pi} \widehat{S}_n(k_1, \varphi_{k_1}) \cdot \widehat{S}_n^*(k_2, \varphi_{k_1} + \psi) \ d\varphi_{k_1}$$

$$\xrightarrow{N \to \infty} \frac{1}{4\pi} \sum_{l=0}^{\infty} P_l(\cos \psi) \sum_{m=-l}^{l} A_{lm}(k_1) \cdot A_{lm}^*(k_2) + \zeta(k_1, k_2, \psi)$$

$$=: C(k_1, k_2, \psi),$$

is derived in Appendix A.1. captured in the additional term $\zeta(k_1, k_2, \psi)$ in (2.8), and its asymptotic expression as $N \to \infty$ tions are corrupted with noise, $C_N(k_1, k_2, \psi)$ is a biased estimator of $C(k_1, k_2, \psi)$. The bias is rotation group SO(3). $C(k_1, k_2, \psi)$ is a nonlinear quadratic function of $\widehat{\rho}(\mathbf{k})$. When the projecless autocorrelation function of the Fourier transform $\widehat{
ho}(k)$ in the frequency domain over the where $P_l(\cdot)$ is the Legendre polynomial of degree l and $C(k_1, k_2, \psi)$ is the asymptotic noise-

denote the estimated $C(k_1, k_2, \psi)$. (PCA) [43, 44]. In addition, for images modified by the contrast transfer functions, one can use covariance Wiener filtering (CWF) for the estimation [10]. We shall use $\widetilde{C}(k_1, k_2, \psi)$ to efficiently estimated from noisy images using the fast steerable principal component analysis and mean of the clean projection images. The covariance matrix and mean image can be Alternatively, $C(k_1, k_2, \psi)$ can be computed from the rotation-invariant covariance matrix The direct computation of the covariance $C_N(k_1, k_2, \psi)$ via (2.8) has high complexity.

degree l, using orthogonality of Legendre polynomials [21, 22], Kam further computed the contribution of the subspace of all spherical harmonics with

(2.9)
$$C_{l}(k_{1}, k_{2}) = 2\pi(2l+1) \int_{0}^{\pi} C(k_{1}, k_{2}, \psi) \cdot P_{l}(\cos \psi) \cdot \sin \psi \, d\psi$$
$$= \sum_{m=-l}^{l} A_{lm}(k_{1}) \cdot A_{lm}^{*}(k_{2}) .$$

Discretizing k into U levels, $k \in \{u_1, u_2, \dots, u_U\}$, the (discretized) l-subspace features $C_l(k_1, k_2)$ can be organized in a $U \times U$ matrix C_l of rank 2l + 1 (assuming $U \ge 2l + 1$):

(2.10)
$$C_{l} = \begin{bmatrix} C_{l}(u_{1}, u_{1}) & C_{l}(u_{1}, u_{2}) & \cdots & C_{l}(u_{1}, u_{U}) \\ C_{l}(u_{2}, u_{1}) & C_{l}(u_{2}, u_{2}) & \cdots & C_{l}(u_{2}, u_{U}) \\ \vdots & \vdots & \ddots & \vdots \\ C_{l}(u_{U}, u_{1}) & C_{l}(u_{U}, u_{2}) & \cdots & C_{l}(u_{U}, u_{U}) \end{bmatrix}.$$

Let A_l denote the $U \times (2l+1)$ matrix of discretized coefficients $\{A_{lm}(k)\}_{lm}$.

(2.11)
$$\mathbf{A}_{l} = \begin{bmatrix} A_{ll}(u_{1}) & A_{l(l-1)}(u_{1}) & \cdots & A_{l(-l)}(u_{1}) \\ A_{ll}(u_{2}) & A_{ll-1}(u_{2}) & \cdots & A_{l(-l)}(u_{2}) \\ \vdots & \vdots & \ddots & \vdots \\ A_{ll}(u_{U}) & A_{l(l-1)}(u_{U}) & \cdots & A_{l(-l)}(u_{U}) \end{bmatrix}.$$

the orthogonal matrices $\{O_l\}_{l=1}^L$ that result in the true but unknown A_l , i.e., such that for all l, $F_lO_l \approx A_l$ (with possible discrepancies due to sampling and noise). Since the Cholesky the orthogonal matrices to reach a consensus so that $\{F_lO_l\}_l$ collectively produce the correct decomposition of C_l is independent for different l, the challenge faced by OMR is to coordinate orthogonal matrix O_l , it holds that $C_l = (A_l O_l^T)(A_l O_l^T)^*$. OMR then attempts to compute aims to recover A_l from the Cholesky decomposition of C_l : $C_l = F_l F_l^*$ We then have $C_l = A_l A_l^*$, where A_l is real for even l and purely imaginary for odd l. OMR aims to recover A_l from the Cholesky decomposition of C_l : $C_l = F_l F_l^*$ [9]. The matrix Fourier transform $\widehat{\rho}(\mathbf{k})$ via (2.4). F_l returned by the Cholesky decomposition is in general different from A_l since, for any

the recovered $\tilde{\rho}(r)$ generally has negative values, leading to additional reconstruction errors. ensure the recovered density $\tilde{\rho}(r)$ corresponds to a nonnegative physical density. As a result, determining the density map $\rho(r)$, there is no easy way to impose constraints on $\{O_l\}_{l=1}^L$ to OMR method is unstable. Additionally, since the orthogonal matrices $\{O_l\}_{l=1}^L$ are coupled in orientation based on the retrieved $\{O_i\}_{i=1}^L$ generally contains error. For these reasons, the merge the results for a completed O_l . However, the retrieval of $\{O_l\}_{l=1}^L$ from a single image other column of O_l , and the relative orientation associated with one of the images is needed to projection images to retrieve $\{O_l\}_{l=1}^L$. Each projection image can be used to determine every an improved OMR by projection matching (OMR-PM) that requires (at least) two denoised usually unavailable and thus have limited applicability [9]. Levin et al. [24] later introduced a nonconvex problem without a known closed-form solution and the estimated relative The earlier OMR methods rely on additional information about the density map that is

- Fourier autocorrelations to $\rho(r)$ as well. the derived connection between spatial and Fourier autocorrelations, we can finally link the and spatial autocorrelation features that are linear and quadratic functionals of $\rho(r)$. Using constraints and matches a reference projection image. To this end, we propose spatial radial orthogonal matrices on the spatial density map that satisfies the nonnegative summation the orthogonal matrices $\{O_l\}_{l=1}^L$ with respect to the recovered density $\tilde{\rho}(r)$ using closed-form solutions. Starting from an initialization density, we then seek a consensus among the alternate between recovering ho(r) subject to nonnegative summation constraints and updating terms of both the density map $\rho(r)$ and the orthogonal matrices $\{O_l\}_{l=1}^L$. This allows us to Spatial features for the MoM. We propose to formulate the recovery problem in
- same norm k: 3.1. Spatial radial features. From the Fourier slices $\{\widehat{S}_n\}_n$, we compute the first-order moment of the Fourier transform $\widehat{\rho}(k)$ by averaging $\widehat{S}_n(k)$ over all directions of k with the

$$(3.1) M_N(k) = \frac{1}{N} \sum_{n=1}^{N} \frac{1}{2\pi} \int_0^{2\pi} \widehat{S}_n(\mathbf{k}) d\varphi$$

$$\xrightarrow{N \to \infty} \frac{1}{4\pi k^2} \int_0^{2\pi} \int_0^{\pi} \widehat{\rho}(\mathbf{k}) \cdot k^2 \sin \theta_{\mathbf{k}} d\varphi_{\mathbf{k}} d\theta_{\mathbf{k}} = \underbrace{\iiint}_{=:M(k),} \frac{\sin(kr)}{kr} \rho(\mathbf{r}) d\mathbf{r}$$

spatial radial features. Fourier radial feature $M_N(k)$ in (3.1). Orthogonality of the sine functions yields the sought where φ is the azimuth angle of k in the Fourier slice \widehat{S}_n . The detailed derivation of (3.1) is given in Appendix D. As derived in Appendix A.2, debiasing is not needed for the (linear)

radius r is given by Spatial radial features. The integration of the 3D density map $\rho(r)$ on the sphere with

$$(3.2) W(r) = \frac{2r}{\pi} \int_0^\infty k \cdot M(k) \cdot \sin(kr) \ dk = \iiint \rho(\tilde{\boldsymbol{r}}) \cdot \delta(r - \tilde{r}) \ d\tilde{\boldsymbol{r}} \ .$$

in the real space linear functional of the density map $\rho(r)$. We additionally compute the total mass W_{ρ} of $\rho(r)$ Radial feature extraction is summarized in Algorithm 3.1. The radial feature W(r) is a

Algorithm 3.1. Spatial radial feature extraction.

ORTHOGONAL MATRIX RETRIEVAL WITH SPATIAL CONSENSUS

Require: The collection of 2D projection images $\{S_n | n = 1, ..., N\}$.

- 1: Compute $\hat{S}_n(k,\varphi)$ from S_n using nonuniform FFT.
- 2: Estimate the first-order moment $M_N(k)$ in (3.1), and use it to approximate M(k)
- 3: Compute the radial feature W(r) in (4.5).
- 4: Return W(r).

$$W_{\rho} = \iiint \rho(\mathbf{r}) d\mathbf{r} = \int_{0}^{\infty} W(r) dr,$$

defined in (3.1) into (3.2). which is a linear constraint on ho(r), and W(r) can be evaluated from data by plugging $M_N(k)$

real spherical harmonics $Y_{lm}(\cdot)$ in the spatial domain, 3.2. Spatial autocorrelation features. We first expand the density map $\rho(r)$ using the

(3.4)
$$\rho(\mathbf{r}) = \sum_{l=0}^{\infty} \sum_{m=-l}^{l} B_{lm}(\mathbf{r}) \cdot Y_{lm}(\theta_{\mathbf{r}}, \varphi_{\mathbf{r}}),$$

where (θ_r, φ_r) is the angular direction of r, $B_{lm}(r)$ is the spatial spherical harmonic expansion coefficient given by

$$(3.5) B_{lm}(r) = \iiint \rho(\tilde{r}) \cdot \delta(r - \tilde{r}) \cdot Y_{lm}(\theta_{\tilde{r}}, \varphi_{\tilde{r}}) \cdot \sin \theta_{\tilde{r}} d\tilde{r} d\theta_{\tilde{r}} d\varphi_{\tilde{r}},$$

where $\delta(\cdot)$ is the Dirac impulse. We then have the following definition. Spatial autocorrelation feature. The inner product of the spherical harmonic coefficient vectors $\{B_{lm}(r_1)\}_m$ and $\{B_{lm}(r_2)\}_m$ is given by

(3.6)
$$E_l(r_1, r_2) = \sum_{m=-l}^{l} B_{lm}(r_1) \cdot B_{lm}(r_2).$$

We call $E_l(r_1, r_2)$ the spatial autocorrelation feature in that we can compute the autocorrelation function $E(r_1, r_2, \psi)$ from it as follows:

(3.7)
$$E(r_1, r_2, \psi) = \sum_{l=0}^{\infty} E_l(r_1, r_2) \cdot P_l(\cos \psi)$$

$$= \frac{1}{2\pi r_1^2 r_2^2} \iiint \int \int \int \int \rho(\tilde{\mathbf{r}}_1) \cdot \rho(\tilde{\mathbf{r}}_2) \cdot \delta(r_1 - \tilde{r}_1) \cdot \delta(r_2 - \tilde{r}_2) \cdot \delta(\psi_{\tilde{\mathbf{r}}_1, \tilde{\mathbf{r}}_2} - \psi) \ d\tilde{\mathbf{r}}_1 d\tilde{\mathbf{r}}_2,$$

from the autocorrelation function in (3.7). spatial correlation function calculated from the projection images in [22] which is different detailed derivation is given in Appendix B. We note that Kam proposed a more complicated where $\psi_{\tilde{r}_1,\tilde{r}_2}$ is the angle between \tilde{r}_1 and \tilde{r}_2 , $\psi \in [0,\pi]$, and $E(r_1,r_2,\psi)$ is the autocorrelation function of the density map $\rho(r)$ in the spatial domain over the rotation group SO(3). The

Suppose r is sampled from $\{v_1, v_2, ..., v_V\}$. We group the (discretized) spatial autocorrelations into a $V \times V$ matrix \mathbf{E}_l of rank at most 2l+1 (assuming $V \geq 2l+1$),

(3.8)
$$E_{l} = \begin{bmatrix} E_{l}(v_{1}, v_{1}) & E_{l}(v_{1}, v_{2}) & \cdots & E_{l}(v_{1}, v_{V}) \\ E_{l}(v_{2}, v_{1}) & E_{l}(v_{2}, v_{2}) & \cdots & E_{l}(v_{2}, v_{V}) \\ \vdots & \vdots & \ddots & \vdots \\ E_{l}(v_{V}, v_{1}) & E_{l}(v_{V}, v_{2}) & \cdots & E_{l}(v_{V}, v_{V}) \end{bmatrix}$$

According to the definition in (3.6), we can write E_l as

$$(3.9) E_l = B_l B_l^T,$$

where \boldsymbol{B}_l is a $V \times (2l+1)$ matrix

(3.10)
$$\boldsymbol{B}_{l} = \begin{bmatrix} B_{ll}(v_{1}) & B_{l(l-1)}(v_{1}) & \cdots & B_{l(-l)}(v_{1}) \\ B_{ll}(v_{2}) & B_{l(l-1)}(v_{2}) & \cdots & B_{l(-l)}(v_{2}) \\ \vdots & \vdots & \ddots & \vdots \\ B_{ll}(v_{V}) & B_{l(l-1)}(v_{V}) & \cdots & B_{l(-l)}(v_{V}) \end{bmatrix}$$

The matrix B_l contains the spherical harmonic coefficients $\{B_{lm}(r)\}_{lm}$ of $\rho(r)$ in the spatial

equation [25], $\rho(r)$. We begin by expanding the plane wave $e^{i\langle k,r\rangle}$ in spherical harmonics via the Rayleigh Fourier expansion coefficients $A_{lm}(k)$ in (2.4) can also be computed using the density map cients of $\rho(\mathbf{r})$ and $\hat{\rho}(\mathbf{k})$. Just like the above spatial expansion coefficients $B_{lm}(r)$ in (3.5), the transform can be derived from the connection between spherical harmonic expansion coeffiautocorrelations are related to Fourier autocorrelations via a spherical Bessel transform. This Connection between spatial and Fourier autocorrelations. The proposed spatial

$$e^{i\langle \mathbf{k}, \mathbf{r} \rangle} = 4\pi \sum_{l=0}^{\infty} \sum_{m=-l}^{l} i^{l} \cdot j_{l}(kr) \cdot (Y_{l}^{m})^{*}(\theta_{\mathbf{k}}, \varphi_{\mathbf{k}}) \cdot Y_{l}^{m}(\theta_{\mathbf{r}}, \varphi_{\mathbf{r}}),$$

harmonic. We then expand $\hat{\rho}(\mathbf{k})$ using the complex $Y_l^m(\cdot)$, where $j_l(kr)$ is the spherical Bessel function of order l and $Y_l^m(\cdot)$ is the *complex* spherical

$$\widehat{\rho}(\mathbf{k}) = \sum_{l=0}^{\infty} \sum_{m=-l}^{l} A_l^m(k) \cdot Y_l^m(\theta_{\mathbf{k}}, \varphi_{\mathbf{k}}),$$

(2.3), (3.11), and (3.12), we get where $A_l^m(k)$ are different from real spherical harmonic coefficients $A_{lm}(k)$ in (2.4). Combining

$$A_l^m(k) = 4\pi \left(\mathfrak{i}^l\right)^* \cdot \iiint \rho(\boldsymbol{r}) \cdot j_l(k\boldsymbol{r}) \cdot (Y_l^m)^*(\theta_{\boldsymbol{r}}, \varphi_{\boldsymbol{r}}) \; d\boldsymbol{r} \, .$$

Expressing $A_{lm}(k)$ in terms of $A_l^m(k)$, we compute

$$A_{lm}(k) = 4\pi \left(rac{i^l}{}
ight)^* \cdot \int \int \int
ho(m{r}) \cdot j_l(kr) \cdot Y_{lm}(heta_{m{r}}, arphi_{m{r}}) \; dm{r} \, .$$

Putting together (3.5) and (3.14), we obtain the following proposition

of $\widehat{
ho}(m{k})$ are related by the following spherical Bessel transforms: The spherical harmonic coefficients $(B_{lm}(r))_{l,m}$ of $\rho(r)$ and $(A_{lm}(k))_{l,m}$

(3.15)
$$B_{lm}(r) = \frac{1}{2\pi^2 (i^l)^*} \int_0^\infty A_{lm}(k) \cdot j_l(kr) \cdot k^2 dk$$

(3.16)
$$A_{lm}(k) = \int_0^\infty 4\pi (i^l)^* \cdot B_{lm}(r) \cdot j_l(kr) \cdot r^2 dr,$$

spherical harmonic coefficient of the Fourier transform $\widehat{\rho}(\mathbf{k})$. where $B_{lm}(r)$ is the spherical harmonic coefficient of the density map $\rho(\mathbf{r})$ and $A_{lm}(k)$ is the

Fourier autocorrelation features as follows: Using the spherical Bessel transforms in Proposition 3.1, we can connect the spatial and

$$(3.17) E_l(r_1, r_2) = \frac{1}{4\pi^4} \int_0^\infty \left(\int_0^\infty C_l(k_1, k_2) \cdot j_l(k_1 r_1) k_1^2 dk_1 \right) \cdot j_l(k_2 r_2) k_2^2 dk_2.$$

(3.18)
$$C_l(k_1, k_2) = 8\pi^2 \int_0^\infty \left(\int_0^\infty E_l(r_1, r_2) \cdot j_l(k_1 r_1) r_1^2 dr_1 \right) \cdot j_l(k_2 r_2) r_2^2 dr_2$$

Fourier autocorrelation features according to (3.17). As summarized in Algorithm 3.2, we extract the spatial autocorrelation features from the

Fourier autocorrelation feature $C_l(k_1, k_2)$ as a quadratic functional of $\rho(\mathbf{r})$. feature $E_l(r_1, r_2)$ in (3.6) is a quadratic functional of $\rho(r)$. Using (3.18), we can also write the lation features must be expressed as functions of $\rho(r)$. The proposed spatial autocorrelation To formulate the reconstruction problem in terms of the density map $\rho(r)$, the autocorre-

in (2.11) that contains the coefficients $\{A_{lm}(k)\}_{lm}$ can be computed as spatial domain and the frequency sampling radii $k \in \{u_1, \ldots, u_U\}$. The $U \times (2l+1)$ matrix A_l denote the GLQ weights associated with the GLQ sampling locations $r \in \{v_1, \dots, v_V\}$ in the spherical Bessel transform in (3.16) by Gauss-Legendre quadrature (GLQ). Let $\{q_1, \dots, q_V\}$ It is convenient to formulate (3.18) in matrix form. To this end, we approximate the

$$A_l = Q_l^* B_l \,,$$

Algorithm 3.2. Spatial autocorrelation feature extraction.

Require: The collection of 2D projection images $\{S_n | n = 1, ..., N\}$.

1: Compute $\hat{S}_n(k,\varphi)$ from S_n using nonuniform FFT.

- Estimate the Fourier autocorrelation function $C_N(k_1, k_2, \psi)$ in (2.8).
- 3: Calculate the debiased and denoised $\widetilde{C}(k_1,k_2,\psi)$, and use it to approximate $C(k_1,k_2,\psi)$.
- Extract the *l*-subspace features $C_l(k_1, k_2)$ in (2.9), and save them in a matrix C_l
- Compute the autocorrelation feature matrix E_l :
- Transform each column of C_l according to (3.15), and save the transformed matrix as
- Transform each row of C'_l according to (3.15), and save the transformed matrix as E_l .

$$(3.20) Q_l(v_i, u_j) = \left(4\pi \mathbf{i}^l \cdot j_l(v_i u_j) \cdot v_i^2\right) \cdot q_i$$

We can then write the Fourier autocorrelation features C_l as

3.21)
$$C_l = AA_l^* = Q_l^* B_l B_l^T Q_l = Q_l^* E_l Q_l.$$

correlations E_l to encourage consistency between the orthogonal matrices and the estimate We will use this link between Fourier autocorrelations C_l and $\rho(r)$ through the spatial auto-

points within a radius of $\frac{G-1}{2}$ from the origin, leading to the following discrete representation: center of mass at the central cell (0,0,0). The 3D density map $\rho(r)$ is then sampled at grid G is odd and let the discrete coordinates range from -(G-1)/2 to (G-1)/2. We fix the the 3D spatial domain is discretized into a $G \times G \times G$ Cartesian grid. For simplicity we assume 4. Parametric density map. Since the density map has finite spatial support in practice,

$$\rho(\mathbf{r}) = \sum_{d=1} w_d \cdot h(\mathbf{r} - \boldsymbol{\mu}_d),$$

location. By abuse of notation, for simplicity we also use $\rho(r)$ to denote the parametric density associated with the sampling grid, and $w_d \ge 0$ is the weight corresponding to the dth sampling of the dth sampling location on the Cartesian grid, $h(\cdot)$ is a nonnegative bump function where D is the number of sampling locations, $\boldsymbol{\mu}_d = [\mu_d(x) \ \mu_d(y) \ \mu_d(z)]^T \in \mathbb{R}^3$ is the coordinate

let \mathcal{M} denote the set of grid points. We then have for support estimation and pruning. Let $\overline{S}(x,y)$ denote the denoised reference projection, and which makes it no longer suitable to estimate features. MFVDM (like many other denoising methods) introduces unknown bias to the denoised image reference projection using the multifrequency vector diffusion maps (MFVDM) [15]. However, is relatively high, the images can be denoised via a low-pass filter. Here we shall denoise the away the grid points that are inconsistent with this reference projection. When the SNR level projection image as the reference projection with an identity rotation matrix R=I and prune Reference projection. To reduce the computational complexity, we can choose an arbitrary Notwithstanding, it can still be used

1.2)
$$\mathcal{M} = \left\{ \boldsymbol{\mu}_d \mid \overline{S}(\mu_d(x), \mu_d(y)) > \overline{s}, \text{ and } \|\boldsymbol{\mu}_d\|_2 \le \frac{G - 1}{2} \right\},$$

orthogonal matrices on the spatial density map. as additional linear features that play an important role in forming the consensus among the image $\overline{S}(x,y)$. As discussed later in section 5, we also use the denoised reference projection ≥ 0 is a threshold chosen to filter out those small perturbations in the denoised

harmonic bandwidth. We use the isotropic Gaussian function The bump function $h(\cdot)$ in (4.1) should be isotropic and have a controlled effective spherical

(4.3)
$$h(\mathbf{r}) = \frac{1}{(2\pi)^{\frac{3}{2}} \tau^3} \exp\left(-\frac{1}{2} \frac{\|\mathbf{r}\|_2^2}{\tau^2}\right),$$

weights $\{w_d \mid d=1,\ldots,D\}$ in the sampled discrete representation (4.1). The problem of reconstructing the 3D density map $\rho(r)$ is then equivalent to recovering the and are available in closed form [2], enabling efficient computation of autocorrelation features rotation invariant. Its spherical harmonic coefficients decay exponentially with increasing l $\tau = \frac{\sqrt{3}}{2}$ empirically yielded optimal performance. The isotropic Gaussian $h(\cdot)$ is conveniently where τ is the usual width parameter. Assuming that the grid cell has size $1 \times 1 \times 1$, setting

of real spherical harmonics as Using the parametric density map defined by (4.1) and (4.3), we can write $\rho(\mathbf{r})$ in terms

(4.4)
$$\rho(\mathbf{r}) = \sum_{d=1}^{D} w_d \cdot \sum_{l=0}^{\infty} \sum_{m=-l}^{l} g_{lm}(r, \boldsymbol{\mu}_d) \cdot Y_{lm}(\theta_{\mathbf{r}}, \varphi_{\mathbf{r}}),$$

proposed spatial radial and autocorrelation features in terms of the weight vector $m{w}$ (4.4) is detailed in Appendix C. Plugging (4.4) into (3.2) and (3.6), we finally express the form expression exists, and $Y_{lm}(\cdot)$ is the real spherical harmonic function. The derivation of where $g_{lm}(r, \mu_d)$ is the spherical harmonic expansion coefficient of $h(r-\mu_d)$ for which a closed-

the weight vector $\boldsymbol{w} = [w_1, \dots, w_D]^T$, metric model, there exist real vectors g(r) that let us express W(r) as a linear functional of Parametric spatial radial feature. Assuming that the density follows the introduced para-

$$4.5) W(r) = g(r)^T w.$$

The expression for g(r) is derived in Appendix D.

there exist real vectors $g_{lm}(r)$ such that E_l are quadratics in w, Parametric spatial autocorrelation feature. Similarly, assuming the parametric model holds,

$$E_l(r_1, r_2) = \boldsymbol{w}^T \cdot \left(\sum_{m=-l}^{\iota} \boldsymbol{g}_{lm}(r_1) \cdot \boldsymbol{g}_{lm}^T(r_2) \right) \cdot \boldsymbol{w}.$$

and (4.6) are given in Appendix E. autocorrelations for those triplets $\{(l, r_1, r_2)\}$ that satisfy $r_1 \leq r_2$. The derivations for $g_{lm}(r)$ We note from (4.6) that $E_l(r_1, r_2) = E_l(r_2, r_1)$. Hence we only need to compute spatial

L on the spherical harmonic degree l when $\rho(r)$ in (4.4) can be well approximated by a function of bandwidth L. Summarizing, the domains of r, k, l used to compute the features are $0 \le r \le \frac{G-1}{2}, \ 0 \le k \le \pi$, and $0 \le l \le L$. We approximate the integrals with respect to φ , k, and r (cf. sections 2 and 3) by the GLQ [16, 38]. bandwidth of π . To reduce the computational complexity, we further set a cutoff threshold As mentioned in section 2.1, we assume that $\rho(r)$ has compact support and an effective

on the density, and agreeing with the denoised reference projection. they are mutually consistent, while respecting the nonnegativity and total-mass constraints density, we update the orthogonal matrices simultaneously with the estimated density so that **OMR-SC.** In this section we introduce the proposed OMR-SC. Starting from the initial

reconstruction of $\rho(r)$ is cast as a constrained recovery of the mixture-weight vector w. Since we model the density $\rho(r)$ by a weighted sum (4.1) of Gaussians (4.3) on a grid, the

to simply adapt it to spatial autocorrelations. fashion. We begin by presenting OMR-SC with Fourier autocorrelations and then show how estimate the weight vector \boldsymbol{w} and update the orthogonal matrices $\{\boldsymbol{O}_l\}_{l=1}^L$ in an alternating

autocorrelation matrix E_l in (3.8) can be written as weight vector \boldsymbol{w} . Under the parametric representation in (4.6), the (i,j)th entry of the spatial transform (cf. Proposition 3.1). Let us express the spatial autocorrelations in terms of the correlations are efficiently computed from spatial autocorrelations using the spherical 5.1. OMR-SC using Fourier autocorrelations. As discussed in section 3.3, Fourier auto-

$$E_l(v_i, v_j) = \boldsymbol{b}_l^T(v_i, \boldsymbol{w}) \boldsymbol{b}_l(v_j, \boldsymbol{w}),$$

where $\boldsymbol{b}_l(v, \boldsymbol{w})$ is a vector with (2l+1) elements.

$$oldsymbol{b}_l(v,oldsymbol{w}) \coloneqq \left[egin{array}{c} oldsymbol{g}_{l(l-1)}^T(v)oldsymbol{w} \\ oldsymbol{g}_{l(l-1)}^T(v)oldsymbol{w} \\ \vdots \\ oldsymbol{g}_{l(l-l)}^T(v)oldsymbol{w} \end{array}
ight] = \left[egin{array}{c} oldsymbol{g}_{l(l-1)}^T(v) \\ \vdots \\ oldsymbol{g}_{l(l-l)}^T(v) \end{array}
ight]oldsymbol{w}.$$

The spherical harmonic coefficient matrix B_l of size $V \times (2l+1)$ is then

$$oldsymbol{B}_l = \left[egin{array}{c} oldsymbol{b}_l^T(v_1, oldsymbol{w}) \ oldsymbol{b}_l^T(v_2, oldsymbol{w}) \ dots \ oldsymbol{b}_l^T(v_V, oldsymbol{w}) \end{array}
ight].$$

Each entry in B_l is a linear function of the weight vector w.

Using $A_l = Q_l^* B_l$ in (3.19), we compute the Fourier autocorrelation matrix C_l from w as

(3.21 revisited)
$$C_l = AA_l^* = Q_l^* B_l B_l^T Q_l,$$

the decomposition of C_l is not. We have, for any orthogonal O_l of size $(2l+1)\times(2l+1)$, that recovering w from the linear functionals in A_l is appealing. However, although A_l is unique, from its quadratic functionals C_l is nonconvex and in general challenging, the prospect of where A_l is purely real for even l and purely imaginary for odd l. Since the recovery of w

$$C_l = A_l O_l^T (A_l O_l^T)^* = F_l F_l^*,$$

matrices $\{O_l\}_{l=1}^L$ by alternating between the two tasks. the correct density. When the sampling radii $k \in \{u_1, ..., u_U\}$ are fixed, the matrix A_l only depends on w. We thus jointly estimate the weight vector w and update the orthogonal across the different degrees $l \in \{0,...,L\}$ so that for all l, $F_lO_l = A_l$, and they generate matrix O_l that needs to be recovered. The orthogonal matrices $\{O_l\}_{l=1}^L$ must be consistent where $F_l = A_l O_l^T$. The Cholesky decomposition of C_l yields F_l for some unknown orthogonal

denoised reference projection image. Since we cannot recover the absolute orientation from As mentioned in section 4, we supplement the radial and autocorrelation features by one

is empirically crucial for successful reconstruction. direction R=I without loss of generality. This reference projection acts as a regularizer that uniform unknown view projections, we can associate an arbitrary projection with the viewing

formulate the following nonconvex OMR-SC problem to recover the density in the spatial of the density map represented by w along the z-direction corresponding to \overline{S} . to be recovered, $\overline{S}(x,y)$ is the denoised reference projection, and $P_{w}(x,y)$ is the projection measurement vector that produces the vth radial feature W(v) in (4.5), \boldsymbol{w} is the weight vector Let $B_l(\cdot)$ denote the linear operator on w such that $B_l(w) = B_l$ in (5.2), g(v) is the

$$\begin{aligned} & \underset{\boldsymbol{w}, \{\boldsymbol{O}_l\}_{l=0}^L}{\operatorname{minimize}} & f(\boldsymbol{w}, \boldsymbol{O}_l) \coloneqq \sum_{l=0}^L \|\boldsymbol{F}_l \boldsymbol{O}_l - \boldsymbol{Q}_l^* \boldsymbol{B}_l(\boldsymbol{w})\|_2^2 \\ & + \lambda \cdot \sum_{v=1}^V \left(\boldsymbol{g}(v)^T \boldsymbol{w} - W(v)\right)^2 \\ & + \xi \cdot \sum_{v=1} \left(\boldsymbol{P}_{\boldsymbol{w}}(x, y) - \overline{S}(x, y)\right)^2 \\ & \text{subject to} & 0 \le w_d \le W_\rho, \\ & \sum_{d=1}^D w_d = W_\rho, \\ & O_l^T \boldsymbol{O}_l = \boldsymbol{O}_l \boldsymbol{O}_l^T = \boldsymbol{I}, \quad l \in \{0, \dots, L\}, \end{aligned}$$

integration of $\rho(\mathbf{r})$ in \mathbb{R}^3 equals the total mass W_{ρ} in (3.3), and they can be easily enforced in the spatial domain. Together, they define a convex set \mathcal{S} that is a simplex, in (OMR-SC-F) come from the requirements that the entries of \boldsymbol{w} are nonnegative and the be tuned on some training data acquired under the same setting. The constraints on \boldsymbol{w} where L is the spherical harmonic cutoff degree and λ and ξ are the regularization parameters corresponding to the mean-squared-error (MSE) of radial and projection features which can

(5.4)
$$S = \left\{ \boldsymbol{w} \mid 0 \le w_d \le W_\rho \text{ and } \sum_{d=1}^D w_d = W_\rho \right\}.$$

ab initio model is initialized by solving the following convex problem: SC-F). Noting that both the radial and the projection features are linear measurements, the model from the downsampled projection images and then use it as the initialization to (OMRrectly affects the final solutions w and $\{O\}_{l=0}^L$. We first reconstruct a low-resolution ab initio Initialization. Since the problem in (OMR-SC-F) is nonconvex, the initialization \boldsymbol{w}_0 di-

minimize
$$\sum_{w'=1}^{r} (\boldsymbol{g}(v)^T \boldsymbol{w}' - W(v))^2 + \sum_{x,y} (P_{\boldsymbol{w}'}(x,y) - \overline{S}(x,y))^2$$
(5.5) subject to $0 \le w'_d \le W_\rho$,
$$\sum_{d=1}^{D} w'_d = W_\rho.$$

the minimum l_2 -norm solution [14, 17]. The above (5.5) is an underdetermined linear problem with multiple globally optimal solutions. Such a problem can be solved by the projected gradient descent initialized at $\mathbf{0}$ that favors

random choices for a reference projection generally suffice. points and choose the reconstructions $w, \{O\}_{l=0}^L$ that minimize the MSE of autocorrelation solutions to (5.5). We can thus attempt to solve (OMR-SC-F) starting from multiple initial that we have access to multiple denoised projection images which generally yield different nonconvexity of (OMR-SC-F). To obtain multiple initializations for multiple trials, we note In practice, a single initialization often fails to produce a good reconstruction due to the $\sum_{l=0}^{L} \|F_l O_l - Q_l^* B_l(w)\|_2^2$. For the experiments later in section 6, we find that 10

solving for O_l and w: Given an initialization w_0 , we propose to minimize (OMR-SC-F) by alternating between

• (O-update). Fix w, and update $\{O_l\}_{l=1}^L$ with respect to w:

(5.6)
$$\min \min_{\{O_l\}_{l=0}^{L}} \|F_l O_l - Q_l^* B_l(w)\|_2^2$$
 subject to $O_l^T O_l = O_l O_l^T = I, \quad l \in \{0, ..., L\}.$

[31]This is an orthogonal Procrustes problem, and the closed-form solution for $\{O_l\}_{l=1}^L$ is

$$(5.7) O_l = V_l U$$

where $m{V}_l$ and $m{U}_l$ are obtained from the singular value decomposition of $m{B}_l^T(m{w}) m{Q}_l m{F}_l$

(5.8)
$$\boldsymbol{B}_{l}^{T}(\boldsymbol{w})\boldsymbol{Q}_{l}\boldsymbol{F}_{l}=\boldsymbol{U}_{l}\boldsymbol{\Sigma}_{l}\boldsymbol{V}_{l}^{T}.$$

(w-update). Fix $\{O_l\}_{l=1}^L$, and estimate w with respect to $\{O_l\}_{l=1}^L$.

minimize
$$f_2(\boldsymbol{w}) := \sum_{l=0}^{L} \|F_l O_l - \boldsymbol{Q}_l^* \boldsymbol{B}_l(\boldsymbol{w})\|_2^2$$

 $+ \lambda \cdot \sum_{v=1}^{V} (\boldsymbol{g}(v)^T \boldsymbol{w} - W(v))^2$
 $+ \xi \cdot \sum_{x,y} (P_{\boldsymbol{w}}(x,y) - \overline{S}(x,y))^2$
subject to $0 \le w_d \le W_\rho$,
 $\sum_{d=1}^{D} w_d = W_\rho$.

descent. In the (t+1)th iteration, we have The above (5.9) is a convex problem which can be solved using projected gradient

(5.10)
$$\boldsymbol{w}_{t+1} = \mathcal{P}_{\mathcal{S}}(\boldsymbol{w}_t - \eta \cdot \nabla f_2(\boldsymbol{w}_t)),$$

1413

ORTHOGONAL MATRIX RETRIEVAL WITH SPATIAL CONSENSUS

nonnegative summation constraints, the consensus in the spatial domain is finally reached The consensus among the orthogonal matrices on the density map begins with the initialization Under the requirement that \boldsymbol{w} matches the denoised reference projection subject to iteration, and the operator $\mathcal{P}_{\mathcal{S}}(\cdot)$ projects the gradient descent update onto the convex where $\eta > 0$ is the step size, $\nabla f_2(\boldsymbol{w}_t)$ is the gradient at \boldsymbol{w}_t from the previous th We compute the projection $\mathcal{P}_{\mathcal{S}}(\cdot)$ efficiently using the method proposed in [14].

follows: $G \times G$ the size of the image. The complexities of the proposed OMR-SC steps are then as Computational complexity. Let N denote the number of projection images and autocorrelations is summarized in Algorithm 5.1.

through the alternating updates of $\{O_l\}_{l=1}^L$ and w. The proposed OMR-SC with Fourier

- (1) Feature extraction. The complexity of feature extraction is $\mathcal{O}(NG^3 + LG^3)$.
- (2) Optimization with respect to $\{O_l\}_{l=1}^L$. The overall complexity of computing $\{O_l\}_{l=1}^L$ per iteration is $\mathcal{O}(L^3(LG+G^2))$.
- (3) Optimization with respect to w. The overall complexity of computing w per iteration is $\mathcal{O}(L^2G^3 + G^3\log G)$.

Algorithm 5.1. OMR with spatial consensus using Fourier autocorrelations (OMR-SC-F).

threshold ς . **Require:** Denoised reference projections $\{\overline{S}_i \mid i=1,\ldots,I\}$, step size η , convergence

- 1: Extract the spatial radial features $\{W(v)\}_v$ and Fourier autocorrelation features $\{C_l\}_l$.
- Perform Cholesky decompositions of Fourier autocorrelation matrices $\{C_l\}_l$.
- 3: **for** $i = \{1, ..., I\}$ **do**
- <u>+</u> Compute the initialization $\mathbf{w}_0(i)$ from the spatial radial features $\{W(v)\}_v$ and the *i*th reference projection S_i .
- 5: **for** $t = \{0, 1, ..., T\}$ **do**
- 6: decomposition. Fix $\boldsymbol{w}_t(i)$, and update $\{\boldsymbol{O}_l(i)\}_l$ with respect to $\boldsymbol{w}_t(i)$ via singular value
- .7 gradient descent. Fix $\{O_l(i)\}_l$, and estimate $w_{l+1}(i)$ with respect to $\{O_l(i)\}_l$ via projected
- 8: if $\frac{\|\mathbf{w}_{t+1}(i) \mathbf{w}_t(i)\|_2}{\|\mathbf{w}_t(i)\|_2} < \varsigma$, then
- 9: Convergence is reached, set $w(i) = w_{t+1}(i)$, and break
- 10: **end if**
- 11: end for
- 12: Save the *i*th set of solutions $\{w(i), \{O_l(i)\}_l\}$.
- 13: end for
- Find the set of solutions that minimizes the MSE of autocorrelation features:

(5.11)
$$\tilde{i} = \arg\min_{i} \sum_{l=0}^{L} ||F_{l}O_{l}(i) - Q_{l}^{*}B_{l}(w(i))||_{2}^{2}$$

15: Return $\tilde{\boldsymbol{w}} = \boldsymbol{w}(i)$.

was reached after ~ 500 iterations of optimizing $\{O_l\}_{l=1}^L$ and \boldsymbol{w} in an alternating fashion. nonuniform FFT of projection images can be parallelized and computed on the fly during data estimate the particle orientations of projection images at every iteration. Additionally, the images once to extract the features, which is more efficient compared to approaches that Detailed derivations are given in Appendix F. We only need to go through the projection For the experiments performed later in section 6, we observed that convergence

- features are much smaller, and the corresponding frequency marching effect is thus weaker. frequency marching effect. By contrast, the differences among the gradient norms of spatial first and given priority during optimization, which gives rise to the aforementioned implicit through the iterations. (degrees) ℓ are much larger than those for higher frequencies at initialization and remain so shows that the gradient norms of Fourier features for lower spherical harmonic frequencies icantly stronger when using Fourier autocorrelations. that this is due to the implicit spherical harmonic frequency marching effect that is signifautocorrelations perform better than spatial autocorrelations (cf. section 6). tocorrelations (OMR-SC-S) is derived in Appendix G. We empirically observe that the Fourier OMR-SC using spatial autocorrelations. This suggests that the low-frequency Fourier features are matched The proposed OMR-SC using spatial au-Indeed, Figure 12 in Appendix G.1 We conjecture
- l. A naïve attempt leads to the following ill-posed optimization problem: difficulty OMR faces is how to relate the orthogonal matrices $\{O_l\}_{l=1}^L$ of the different degrees attempts to recover a set of orthogonal matrices $\{O_l\}_{l=1}^L$ such that $F_lO_l=A_l$. The main as $C_l = A_l A_l^*$. in the frequency domain. The feature matrix C_l and the coefficient matrix A_l are related features $C_l(k_1, k_2)$ in (2.9) are used to recover the spherical harmonic coefficients $\{A_{lm}(k)\}_{lm}$ earlier OMR approach is based on Kam's (autocorrelation) method, where the *l*-subspace 5.3. Comparison with earlier OMR methods. As we briefly discussed in section 2.2, the OMR performs Cholesky decomposition on C_l to produce $C_l = F_l F_l^*$ and

for the recovered (O_l, A_l) to be consistent with the true underlying density. To resolve this, different authors proposed to use different kinds of side information [9, 24]. The orthogonal compute its spherical harmonic coefficients A'_l and recover O_l by replacing A_l with A'_l , extension method [9], for example, assumes a similar 3D structure is known so that we can Since the above (5.12) is an independent problem for different degrees l, there is no reason

5.13)
$$\min_{O_l} \| F_l O_l - A_l' \|_2^2 \text{ for all } l \in \{0, \dots, L\}.$$

at degree l. rotation associated with the second projection, and $D_l^{(\chi)}$ the corresponding Wigner D-matrix $\{O_{l,2}\}_l$ the orthogonal matrices recovered from the second projection, χ the unknown relative least) two denoised projections with estimated relative rotations to compute the orthogonal Such additional information is usually unavailable, which limits the method's practical value. A different approach known as OMR-PM was introduced in [24] which instead relies on (at Let $\{O_{l;1}\}_l$ denote the orthogonal matrices recovered from the first projection, It was shown in [24] that every other column of $O_{l;1}D_l^{(\chi)}$ should equal the

orthogonal matrices $\{O_l\}_{l=1}^L$ are coupled to one another in determining the density map $\rho(r)$ over the rotation group SO(3) which tries to match every other column of $O_{l;1}D_l^{(\chi)}$ and is no easy way to implement the nonnegativity constraint. since, for example, they should result in a nonnegative density, but in this formulation there in the estimated rotation χ , which makes the final merging step unstable. nonconvex problem that does not have a known closed-form solution, this introduces errors final solution $\{O_l\}_{l=1}^L$. Since the retrieval of $\{O_{l,1}\}_l$ (or $\{O_{l,2}\}_l$) from a single projection is a $O_{l,2}$. The estimated rotation χ is then used to merge $\{O_{l,1}\}_l$ and $\{O_{l,2}\}_l$ to produce the corresponding column of $O_{l;2}$. The relative rotation χ is estimated by a dense grid search Additionally, the

autocorrelation features and their relation to Fourier autocorrelations in Proposition 3.1. in recovering the density map and the orthogonal matrices. This is enabled by the new spatial solutions in (5.7). With a suitable initialization as computed in (5.5), OMR-SC is more robust needed to determine the orthogonal matrices, and the updates of $\{O_l\}_{l=1}^L$ have closed-form OMR-SC formulation, together with the appropriate constraints, contains all the information in (5.4). $\rho(\mathbf{r})$ and updating the orthogonal matrices $\{O_l\}_{l=1}^L$ with respect to the recovered density $\tilde{\rho}(\mathbf{r})$. It is thus straightforward to enforce nonnegativity via a projection onto the simplex Our proposed OMR-SC approach alternates between recovering the spatial density map Compared to a single projection used by OMR-PM, the 3D density map in the

with the OMR-PM approach on the recovery of 3D density maps. Experimental results. In this section we compare the proposed OMR-SC approach

- the ball embedded in a $101\times101\times101$ Cartesian grid. mixture of Gaussian components whose means are generated using a 3D random walk We first reconstruct 10 random density maps:² each groundtruth density map is a with 500 steps, and variances are set to 1. The model is further scaled to fit within
- A, respectively. with voxels corresponding to cubes with physical side lengths 2.1672 Å, 2.5 Å, and 1.5 ceptor (CaS) density model from the Electron Microscopy Data Bank [27]; (2) the We then reconstruct three protein density maps: (1) the human calcium-sensing repled and scaled to fit within the ball embedded in a $101 \times 101 \times 101$ Cartesian grid, from their atomic models in the Protein Data Bank. The three models are downsam-(PTCH1) density model. Holliday junction complex (HJC) density model; (3) the human patched 1 protein HJC and PTCH1 maps are synthesized in Chimera [28]

SNR = 0.1 as in the typical low-SNR scenario of UVT, where 101×101 and corrupt them with additive white Gaussian noise (AWGN) so that the resulting density $W_{\rho} = 50$. The 2D projection images are generated from N uniformly distributed 3D Without loss of generality, the density maps are normalized so that the total mass of each As shown in Figure 2, we generate N = 10,000 noiseless projection images of size

$$\text{SNR} = \frac{\text{Power of Signal}}{\text{Power of Noise}} = \frac{\mathbb{E}\left[\sum_{x,y} S(x,y)^2\right]}{\mathbb{E}\left[\sum_{x,y} \epsilon(x,y)^2\right]}.$$

structions is generally limited to several density maps ²Due to the high computational complexity of UVT applications such as cryo-EM, the number of recon-

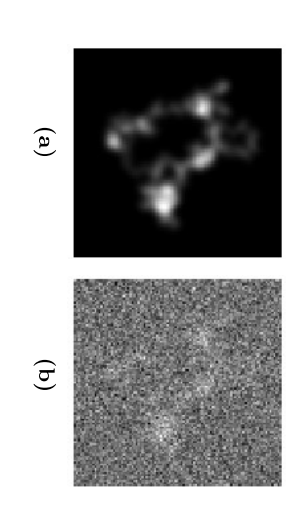


Figure 2. (a) A noiseless 2D projection image. (b) A noisy 2D projection image with SNR = 0.1.

is calculated using the FINUFFT package [4, 5]. and the spherical harmonic bandwidth L=10. The nonuniform FFT of the projection image points for $r \in [0, 50]$, U = 51 uniformly sampled points for the frequency bandwidth $k \in [0, \frac{\pi}{2}]$, of the 3D density and its projection images, $\Phi = 401$ GLQ points for $\varphi \in [0, 2\pi]$, V = 101 GLQ between complexity and accuracy: $k_{\text{max}} = \frac{\pi}{2}$ as the cutoff frequency (approximate bandlimit) cally (through trial and error) determined that the following choices provide a good balance according to the GLQ rule. Using a holdout random density as the training data, we empiri-6.1. Feature extraction. The integrations involved in feature extraction are computed

features is usually larger for higher spherical harmonic degrees. steerable PCA [43]. As shown in Figure 3, the normalized-root-mean-squared-error of the package [36], we calculate the debiased and denoised autocorrelation features C_l via the fast The linear radial features do not need to be debiased or denoised. Using the ASPIRE

the same setting), and they are both set to 1 in OMR-SC-S. both set to 100 (by monitoring the loss on a training random density map generated under the computational complexity. The regularization parameters λ and ξ in (OMR-SC-F) are recovery formulation. As discussed in section 4, we can prune away the sampling locations be used for computing MoM features, they can be used as linear "measurements" in our projection by MFVDM [15]. Although the denoised images contain unknown bias and cannot one denoised reference projection image as additional linear features. We denoise this one $\{\mu_d\}_d$ on the Cartesian grid that are not consistent with the reference projection to reduce Reconstruction of 3D density maps. The proposed OMR-SC approach leverages

solution. As a result, we use all of the same 10 projections in OMR-PM to achieve the best function of OMR-PM is not rotation invariant and depends on the chosen set of projections the "rotation-invariant" MSE of autocorrelation features. On the other hand, the objective resolution reconstruction. Among all the obtained solutions, we choose the one that minimizes every density map. We then refine the ab initio models via OMR-SC again to get the highpling the projection images. Specifically, a $33 \times 33 \times 33$ ab initio model is computed for modeling via OMR-SC, where a low-resolution density map is reconstructed by downsamprojections to perform the reconstructions in parallel. In practice, we first perform ab initio images to compute different initializations for OMR-SC. Here we use 10 randomly selected [24]. Hence it could not be compared across different sets of projections to select the best As discussed in section 5, we can combine spatial radial features with different denoised

ORTHOGONAL MATRIX RETRIEVAL WITH SPATIAL CONSENSUS

Figure 3. Fourier autocorrelation feature \tilde{C}_l is extracted from N=10,000 projection images with SNR=0.1.

(e) NRMSE of \tilde{C}_5 : 0.0197

(f) NRMSE of \vec{C}_{10} : 0.1034

0.5

0.5

(d) NRMSE of \widetilde{C}_1 : 0.0821

from the spherical Bessel expansion coefficients a_{lms} of $A_{lm}(k)$ [11], We also note that OMR-PM uses a different set of autocorrelation features constructed

6.1)
$$A_{lm}(k) = \sum_{s=1}^{C_l} a_{lms} \cdot j_{ls}(k),$$

straightforwardly to use a_{lms} as features, which produces similar performance to $A_{lm}(k)$ based on $A_{lm}(k)$ would still hold in this case. The proposed OMR-SC could also be adapted $A_{lm}(k)$ through a linear spherical Bessel transform, and our previous discussion of OMR-PM where $j_{ls}(k)$ is the normalized spherical Bessel function. We can see that a_{lms} is connected to

corresponding spherical shells with radius k in the frequency domain [18]: and is given by the normalized cross-correlation coefficient between two aligned volumes over It measures the similarity between two volumes (ρ_1, ρ_2) with respect to the spatial frequency A standard reconstruction quality metric in UVT is the Fourier shell correlation (FSC).

(6.2)
$$\operatorname{FSC}(k) = \frac{\sum_{k_i = k} \widehat{\rho}_1(\mathbf{k}_i) \widehat{\rho}_2(\mathbf{k}_i)^*}{\sqrt{\sum_{k_i = k} |\widehat{\rho}_1(\mathbf{k}_i)|^2} \cdot \sqrt{\sum_{k_i = k} |\widehat{\rho}_2(\mathbf{k}_i)|^2}},$$

the ith voxel in the frequency domain. We apply a cutoff threshold of 0.5 on the FSC curve where $\hat{\rho}_1$ and $\hat{\rho}_2$ are the Fourier transforms of the two aligned volumes and k_i corresponds to

Resolutions (in voxel) of recovered random density maps using the OMR-PM and OMR-SC approaches (FSC cutoff threshold =0.5).

OMR-SC-F 8.47 10.80 7.42	OMR-SC-S 13.09	Noisy OMR-PM 34.13 31.55 11.71 21.98 27.32 17.42	OMR-SC-F 6.70 9.62	OMR-SC-S 8.83	Noiseless OMR-PM 11	DJ
17 10.80	.09 15.20	.13 31.55	70 9.62	9.32	11.64 11.90	D1 D2 D3 D4 D5 D6 D7 D8 D9
7.42	7.98	11.71	5.90	8.98	0 7.00	D3
10.98 9.18 6.01 17.51 8.94 12.14 8.45	14.73 10.48 6.45	21.98	7.28 5.94 4.10 10.63 7.48 8.46 5.54	12.06	14.14	D4
9.18	10.48	27.32	5.94	11.33	$11.15 \ 10.95$	D_5
6.01	6.45	17.42	4.10	∞ သ	10.95	D6
17.51	21.37	28.65	10.63	13.39	13.68 9.57	D7
8.94	16.13	$14.03 \ 17.64$	7.48	12.67		D8
12.14	14.14 12.15	17.64	8.46	12.24	11.93	D9
8.45	12.15	26.11	5.54	10.19	21.93	D10

Correlation coefficients of recovered random density maps using the OMR-PM and OMR-SC approaches. Table 2

0.86	0.77		0.71			0.82	0.92	0.71	0.85	OMR-SC-F	
0.67		0.68	0.62	0.80	0.75	0.74	0.85	0.62	0.68	OMR-SC-S	
0.38	0.67	0.77	0.58			0.56	0.78	0.45	0.39		Noisy
0.91		0.91	0.83	0.96	0.96	0.92	0.96	0.84		OMR-SC-F	
0.80	0.79	0.75	0.80	0.73	0.76	0.75	0.83	0.75	0.78		
0.47	0.84	0.86	0.79	0.61	0.75	0.76	0.90	0.69			Noiseless
D10	D9	D8	D7	D6	D5	D4	D3	D2	D1		

groundtruth globally, we calculate another standard metric, the correlation coefficient [1]. to determine the volume resolution [37]. To evaluate how well the reconstruction matches the

formulations and their corresponding optimization procedures. same. As discussed in section 5.3, the performance differences are due to the different problem densities than OMR-PM. The information used by OMR-PM and OMR-SC is essentially the OMR-PM on all the densities. In both cases, OMR-SC-F is more robust across the different than OMR-PM on all the densities. With noise, OMR-SC-F performs significantly better than than OMR-SC-S with spatial autocorrelations. Without noise, OMR-SC-F performs better coefficients. We see that OMR-SC-F with Fourier autocorrelations generally performs better dom density maps using OMR-PM and OMR-SC. Table 2 shows the corresponding correlation **6.2.1. Random density maps.** Table 1 shows the resolutions (in voxel) of recovered ran-

density map well. the bump function (4.3). Despite the model mismatch, the sampling locations of the Cartesian grid and their variances are different from the one in We also note that there is always a mismatch between the parametric density map in (4.1) and ual observation that 3D structures are revealed better by OMR-SC reconstructions in general blurrier. The quantitative correlation coefficients in Table 2 are also consistent with the vis-[local/web 3.45MB]). We can see that the OMR-PM reconstructions are generally much density maps are given in the supplementary material (UVT_SIIMS_Supplementary.pdf in Figures 5 and 6. Additional figures showing the rest of the FSC curves and reconstructed curves in Figure 4 and show the 3D and 2D projection views of the reconstructed density maps groundtruth, since the Gaussian mixtures in the groundtruth are generally not located on Using the first and tenth random densities as representative examples, we plot the FSC OMR-SC is still able to recover the

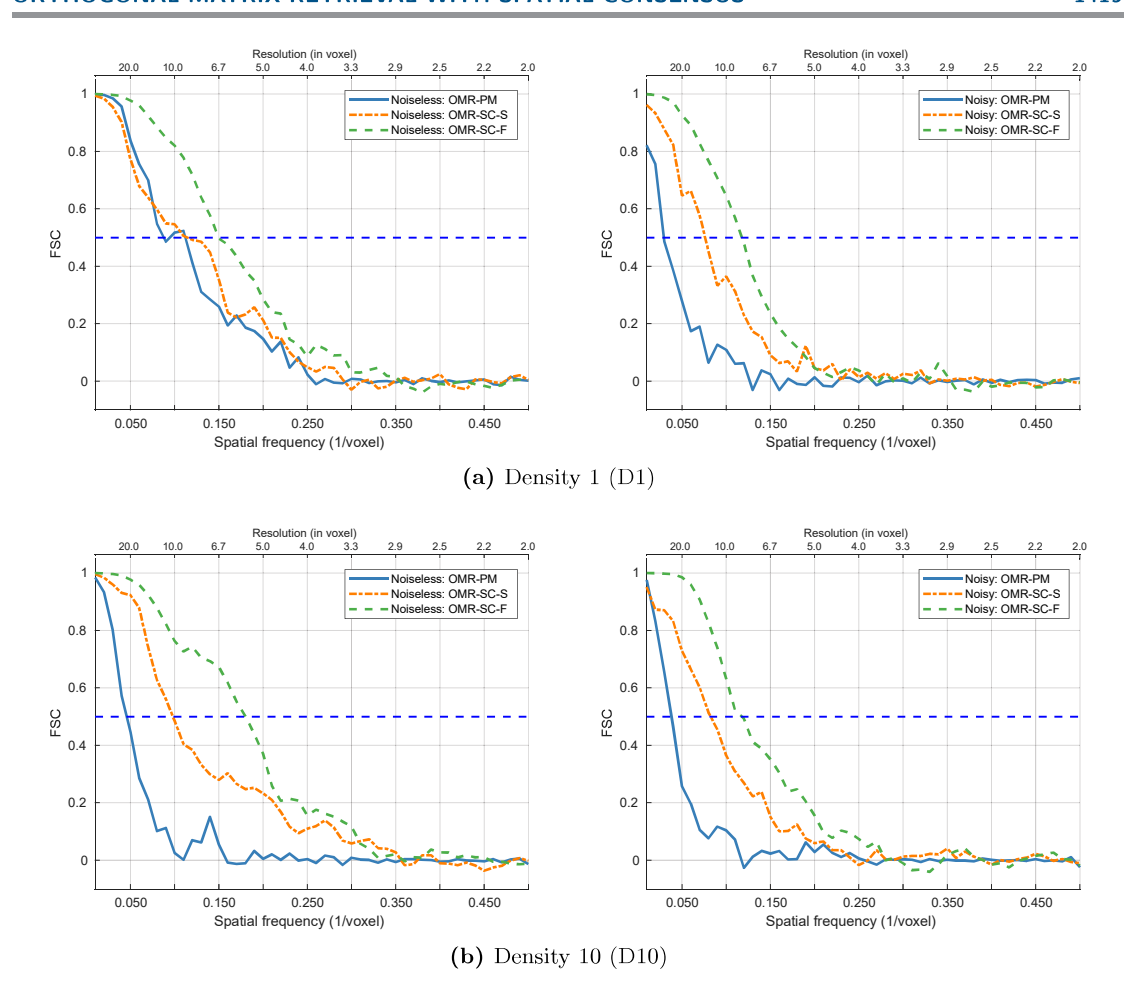


Figure 4. FSC curves of recovered random density maps D1 and D10 using the OMR-PM and OMR-SC approaches in the noiseless case and the noisy case (SNR = 0.1). The cutoff threshold of 0.5 is used to determine the resolution (in voxel).

Due to the nononvexity of the problem, the initialization directly affects the performance of OMR-SC. The proposed initialization scheme draws information from a reference image and spatial radial features. The performances of the ab initio models produced by OMR-SC-F are given in Appendix H. Tables 3 and 4 compare the performances of the OMR-SC-F approaches with the random (R) and proposed (P) initializations. We can see that the proposed initialization scheme generally leads to better performances except on the noisy recovery of the densities D9 and D10.

The nonnegativity constraints are important to the robustness of OMR-SC; they ensure that the orthogonal matrices reach the consensus on a "physical" density map in the spatial domain. Tables 5 and 6 compare the performances of the OMR-SC-F approaches with and without the nonnegativity constraints. In terms of correlation coefficient, we can see that

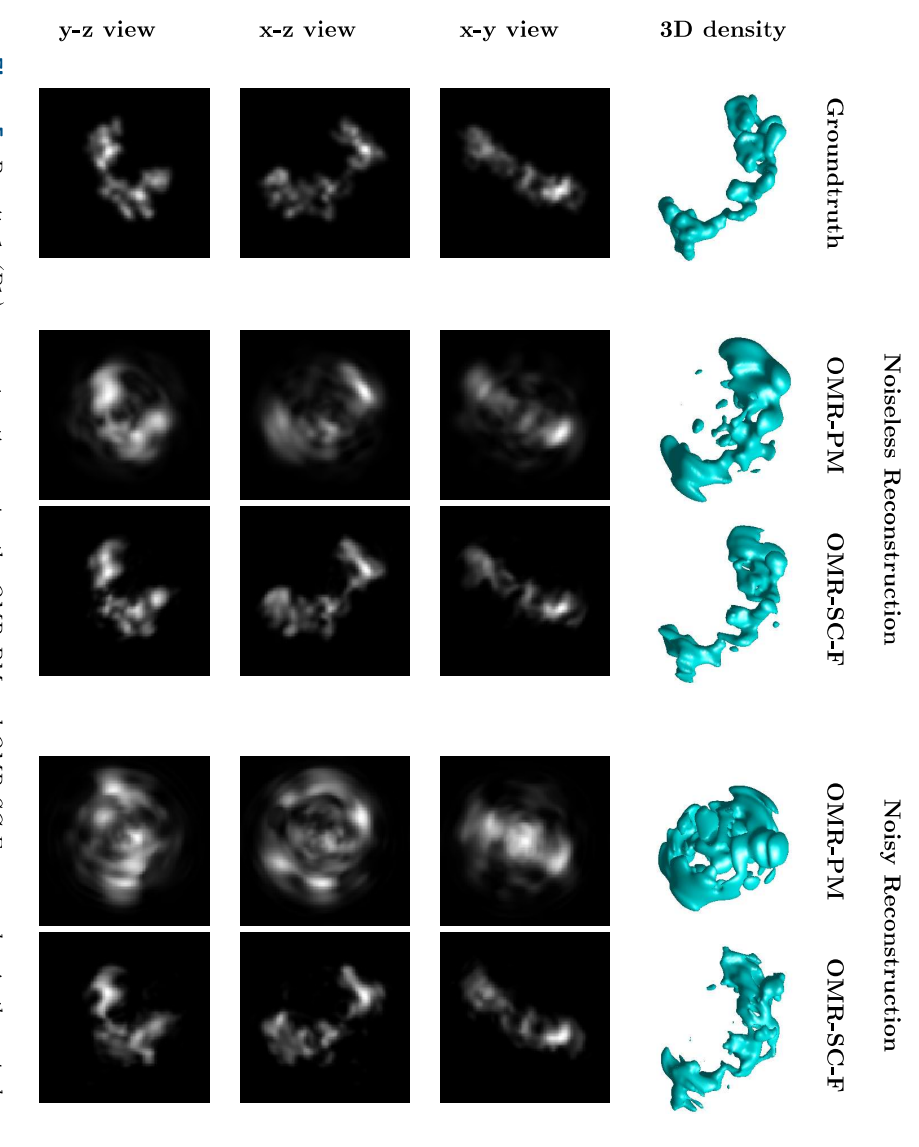
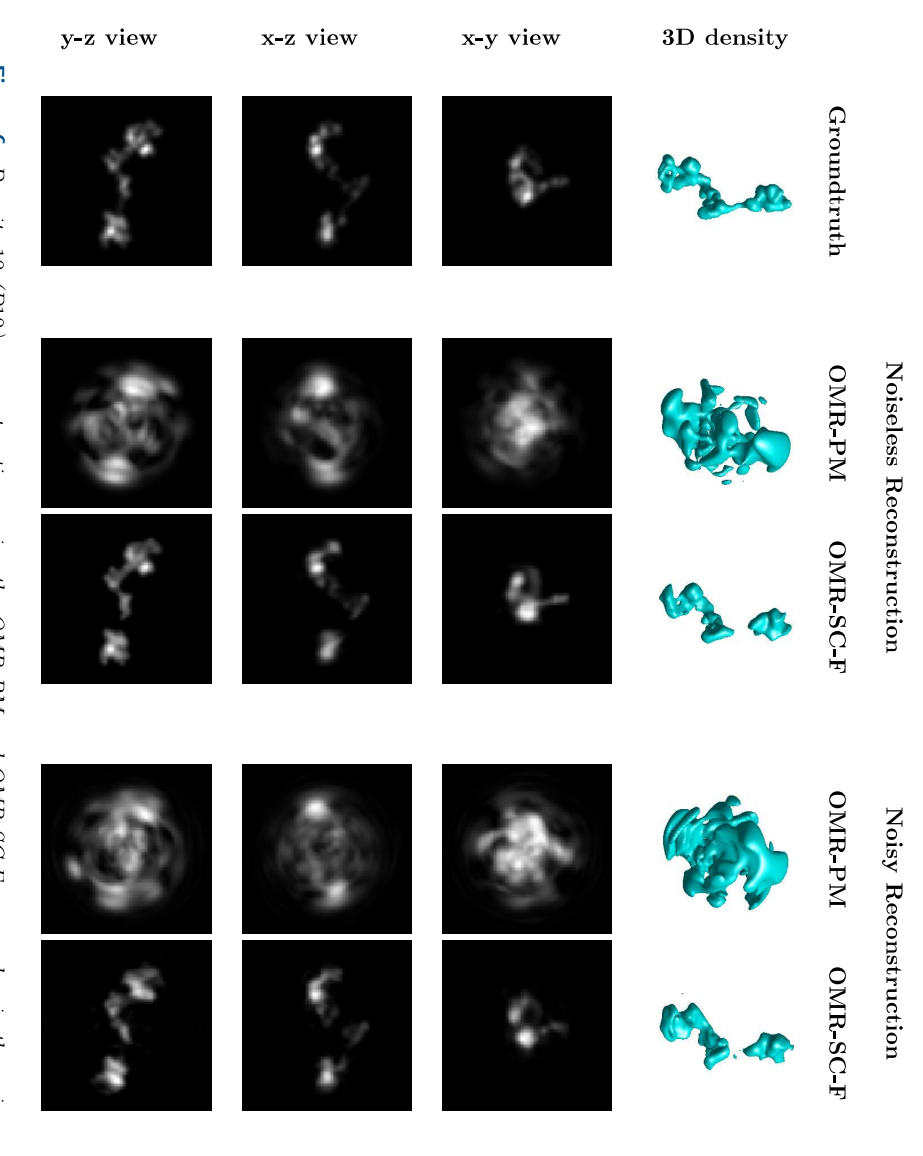


Figure 5. Density 1 (D1): reconstructions using the OMR-PM and OMR-SC-F approaches in the noiseless and the noisy case (SNR = 0.1).

included. OMR-SC-F achieves significantly better performances when the nonnegativity constraints are

uses Fourier autocorrelations. of PTCH1, the OMR-SC-S that uses spatial autocorrelations outperforms the OMR-SC-F that SC performs much better on all three density maps. In particular, for the noisy reconstruction equally well on PTCH1. However, in the noisy case OMR-PM becomes unstable, and OMRcan see that OMR-PM performs better than OMR-SC on CaS and HJC, and they perform show the recovered density maps in 3D and 2D projection views. In the noiseless case, we of recovered protein density maps, Figure 7 shows the FSC curves, and Figures 8, 9, and 10 **6.2.2. Protein density maps.** Table 7 shows the resolutions and correlation coefficients

also show that the proposed initialization and the nonnegativity constraints generally lead to we either used random initializations or removed the nonnegativity constraints. The results better and more robust performances. In terms of correlation coefficient, although OMR-SC-We also compare the performances of the OMR-SC-F approaches in Tables 8 and 9, where



case and the noisy case (SNR = 0.1). Figure 6. Density 10 (D10): reconstructions using the OMR-PM and OMR-SC-F approaches in the noise-

Resolutions (in voxel) of recovered random density maps using the OMR-SC-F approaches with the random (R) and proposed (P) initialization schemes (FSC cutoff threshold = 0.5). Noiseless OMR-SC-F (R) **6.48** 10.99 OMR-SC-F (P) 6.70 **9.62** \square D26.09 \mathbb{D}_3 D_4 7.476.86 D_{5} D6 4.27D7 11.219.43 D_8 12.59D9 5.93D10

Noisy OMR-SC-F OMR-SC-F (P)9.72 **8.47** 10.8018.73**7.23** 7.42 $5.90\ 7.28$ 10.9813.648.835.94 4.10 10.63 7.48**5.97** 6.01 **16.39** 17.51 14.51**9.78** 12.14 8.465.54

PTCH1, it is not as robust as the OMR-SC-F with the constraints. F without the nonnegativity constraints performs better on the particular noisy recovery of

and quadratic functionals of the density map. UVT, we proposed spatial radial and autocorrelation features that can be expressed as linear Conclusion. In an effort to expand the applicability of the method of moments in Via a spherical Bessel transform, the spa-

Correlation coefficients of recovered random density maps using the OMR-SC-F approaches with the random (R) and proposed (P) initialization schemes.

Noisy	Noiseless	
OMR-SC-F (R) 0.78 0.57 OMR-SC-F (P) 0.85 0.71	ss OMR-SC-F (R) 0.90 OMR-SC-F (P) 0.92	
0.78	0.90 0.92	D1 D2
0.57 0.71	0.78 0.84	
0.93 0.92	0.95 4 0.96	D3
0.71 0.82	0.91 6 0.92	D4
0.87 0.89 0.88 0.89	0.90 0.96	D5
0.89 0.89	0.94 0.96	D6
0.71 0.67 0.71 0.85	0.81 0.83	D7
0.67 0.85	0.79 0.91	D8
0.87	0.73 0.91	D9
0.89	0.91 0.91	D10

Table 5

Resolutions (in voxel) of recovered random density maps using the OMR-SC-F approaches with (w/) and without (w/o) nonnegativity constraints (FSC cutoff threshold = 0.5).

8.45	12.14	8.94	17.51	6.01	9.18	10.98	7.42	10.80	8.47	OMR-SC-F (w/o) 8.00 10.00 5.34 00.05 21.52 10.19 10.10 20.79 17.59 10.09 OMR-SC-F (w/) 8.47 10.80 7.42 10.98 9.18 6.01 17.51 8.94 12.14 8.45
5.54	8.46	7.48	10.63	4.10	5.94	7.28	5.90	9.62	6.70	<u>'</u>
6.54	16.16	9.03	15.24	6.27	8.01	10.67	11.16	9.54	8.98	Noiseless OMR-SC-F (w/o) 8.98 9.54 11.16 10.67 8.01 6.27 15.24 9.03 16.16 6.54
D10	D9	D8	D7	D5 D6 D7	D5	D4	D3	D2	D1 D2	

Table 6

without (w/o) nonnegativity constraints. Correlation coefficients of recovered random density maps using the OMR-SC-F approaches with (w/) and

0.86	0.71 0.85 0.77 0.86	0.85	0.71	0.89	0.88	0.82	0.92	$0.71 \ 0.92$	0.85	OMR-SC-F (w/) 0.85
0.76	0.68	0.62	0.70	0.64	0.53	0.22	0.88	0.64	0.74	Noisy OMR-SC-F (w/o)
0.91).91	3 0.91 (0.83	0.96	0.96	0.92	0.96	0.84	0.92	OMR-SC-F (w/) 0.92
0.87	0.68	0.83	0.78	0.75	0.86	0.85	0.76	0.75	0.78	Noiseless OMR-SC-F (w/o) 0.78
D10	D9	D8	D7	D6	D5	D4	D3	D2	D1	

Table 7

Resolutions (Å) and correlation coefficients of recovered protein density maps using the OMR-PM and OMR-SC approaches (FSC cutoff threshold = 0.5).

		Ŧ	Resolution ((Å)	Corr	Correlation co	1 coefficient
		$\overline{\mathrm{CaS}}$	нјс	PTCH1	CaS	HJC	PTCH1
Noiseless	OMR-PM	13.84	26.59	18.92	0.95	0.88	0.86
	OMR- SC - S	16.44	40.26	20.46	0.89	0.74	0.87
	OMR-SC-F	14.04	29.38	16.52	0.93	0.78	0.86
Noisy	OMR-PM	29.49	95.42	44.51	0.77	0.53	0.69
	OMR- SC - S	28.78	38.23	43.73	0.76	0.73	0.74
	OMR-SC-F	16.15	36.82	31.38	0.87	0.73	0.73

sought density. Prior work noted that (under realistic assumptions) the autocorrelation feaorthogonal matrices. Due in part to the functional forms of the used features, recovering the orthogonal matrices. tures determine the spherical harmonic coefficients of the density map up to a set of unknown tial autocorrelations provide a closed-form link between the Fourier autocorrelations and the But that prior work only attempted to recover the a priori uncoupled

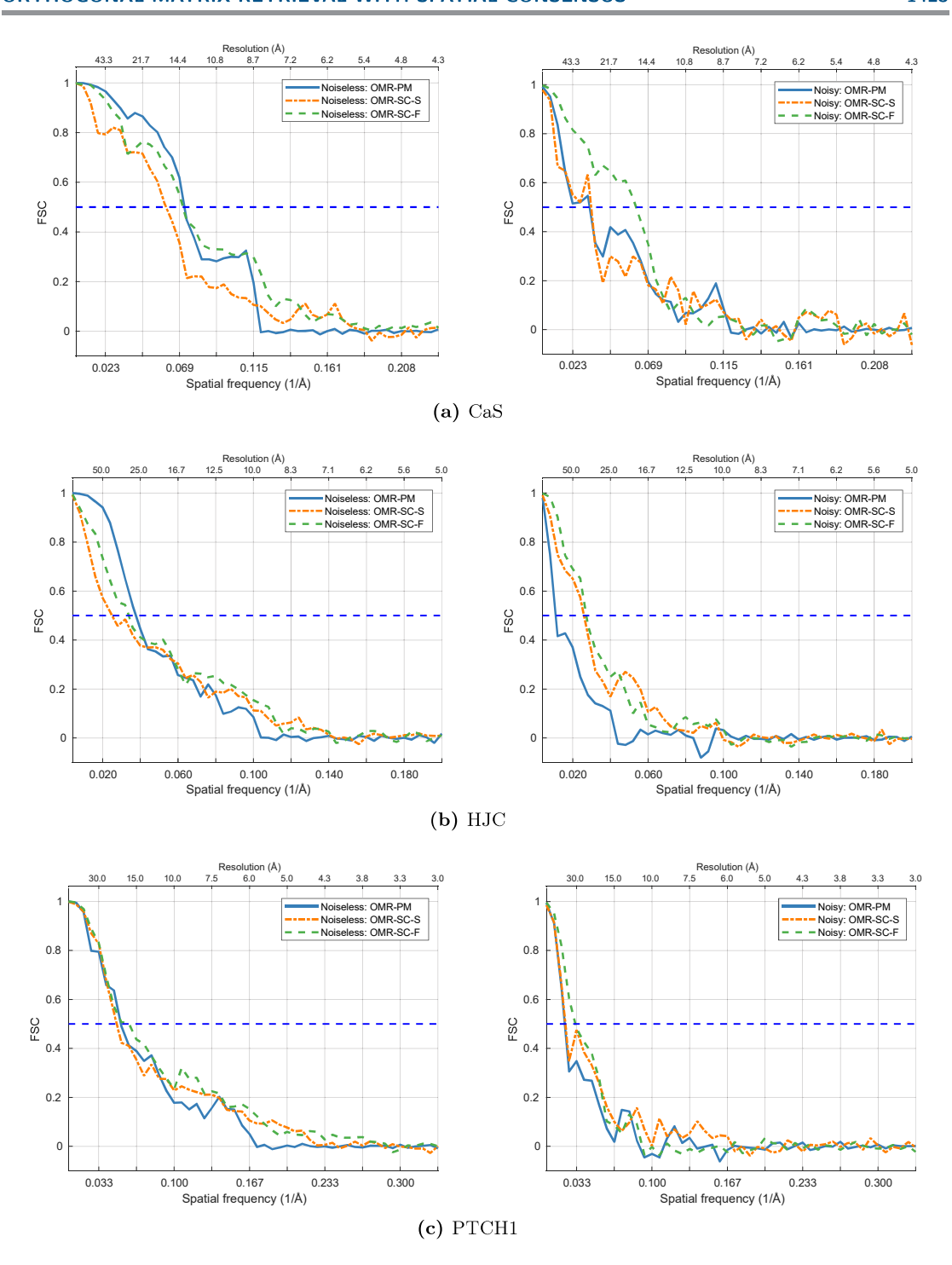


Figure 7. FSC curves of recovered protein density maps using the OMR-PM and OMR-SC approaches in the noiseless case and the noisy case (SNR=0.1). The cutoff threshold of 0.5 is used to determine the resolution (in Å).

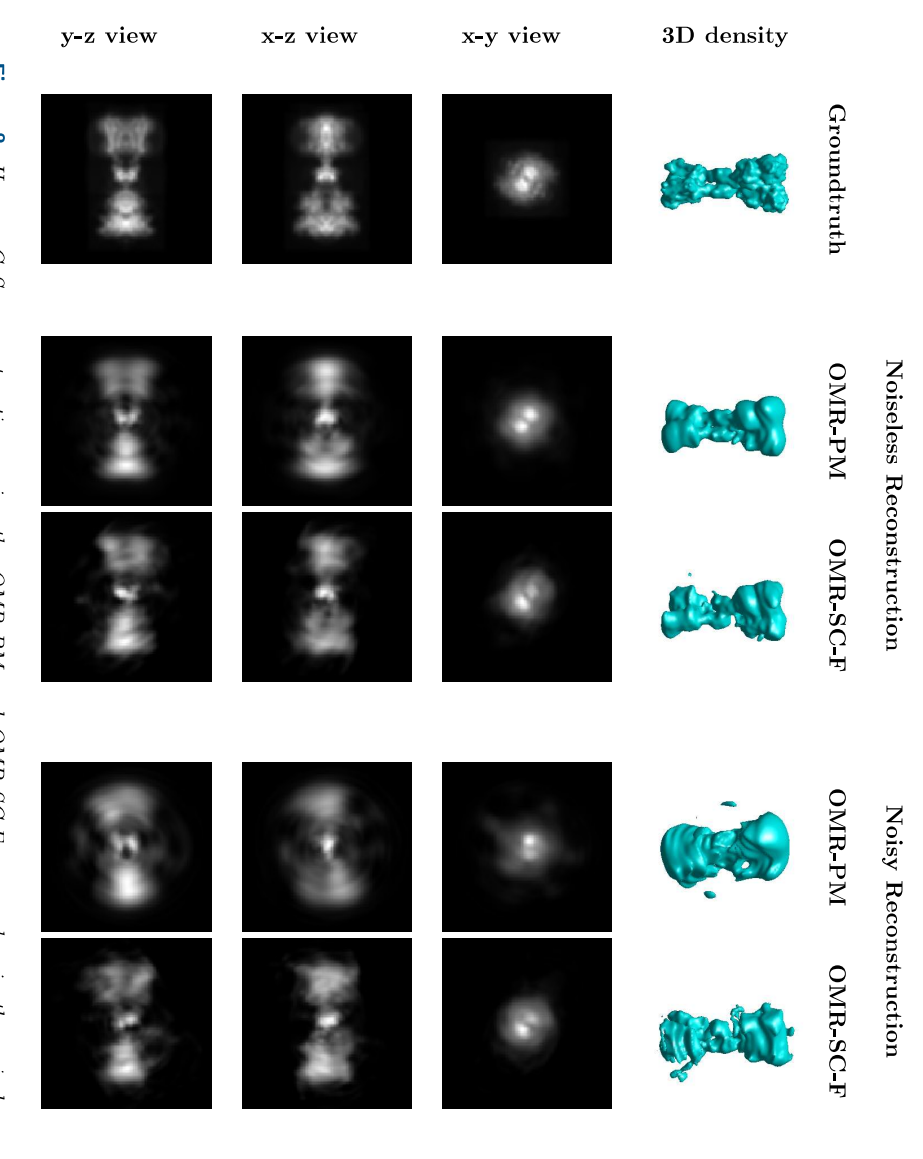
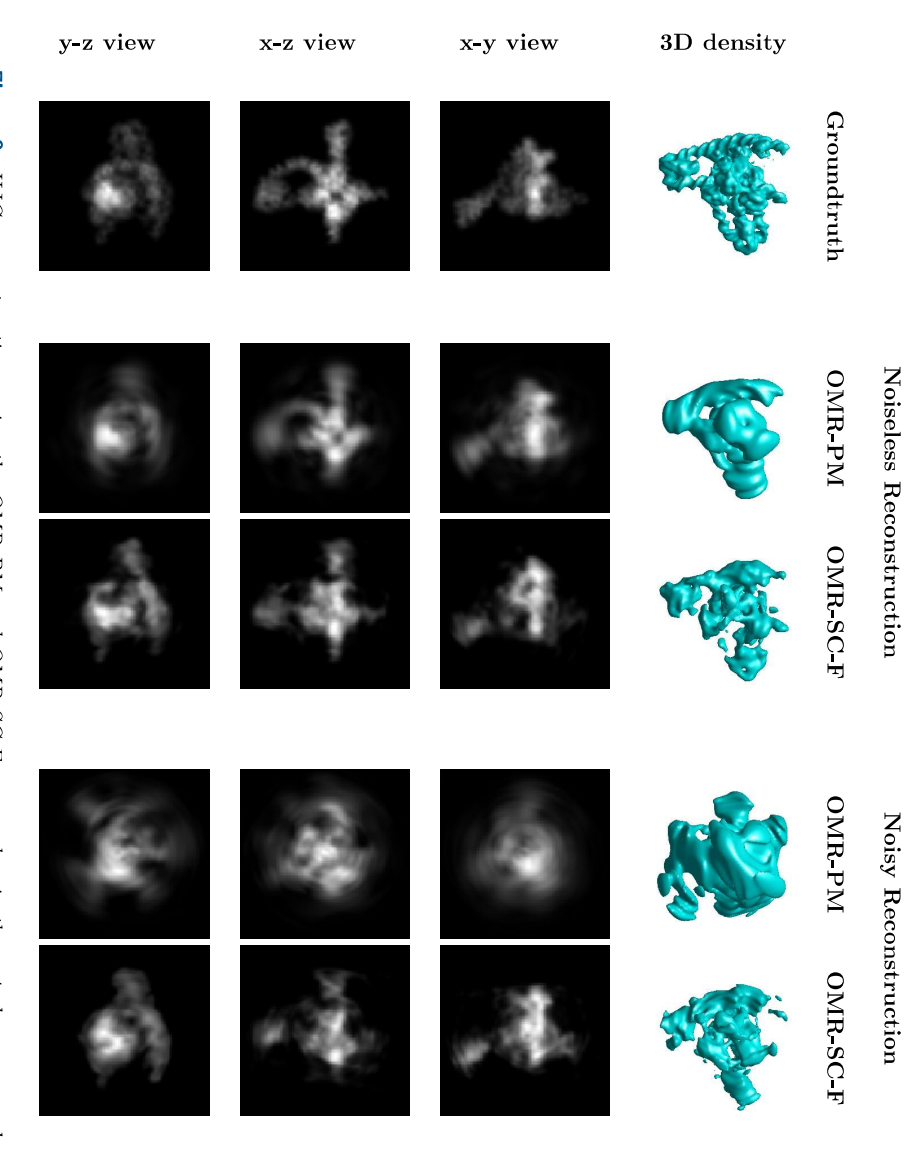


Figure 8. Human CaS: reconstructions using the OMR-PM and OMR-SC-F approaches in the noiseless and the noisy case (SNR = 0.1).

the involved optimization problems. constraints has been challenging. The challenge has been exacerbated by the nonconvexity of correct matrices that "agree" on a proper density estimate that satisfies the problem-specific

bust and performs much better in the the presence of noise than the previous state-of-the-art the denoised reference projection. and the orthogonal matrices in an alternating fashion, constraining the density map to be ciently computable initial density. We then formulated a joint recovery of the density map features, and we greatly alleviated the second, nonconvexity challenge, by designing an effi-(1) nonnegative, (2) compactly supported, (3) of correct total mass, and (4) consistent with In this paper we addressed the first challenge by the newly proposed closed-form spatial Experiments show that the proposed OMR-SC is more ro-

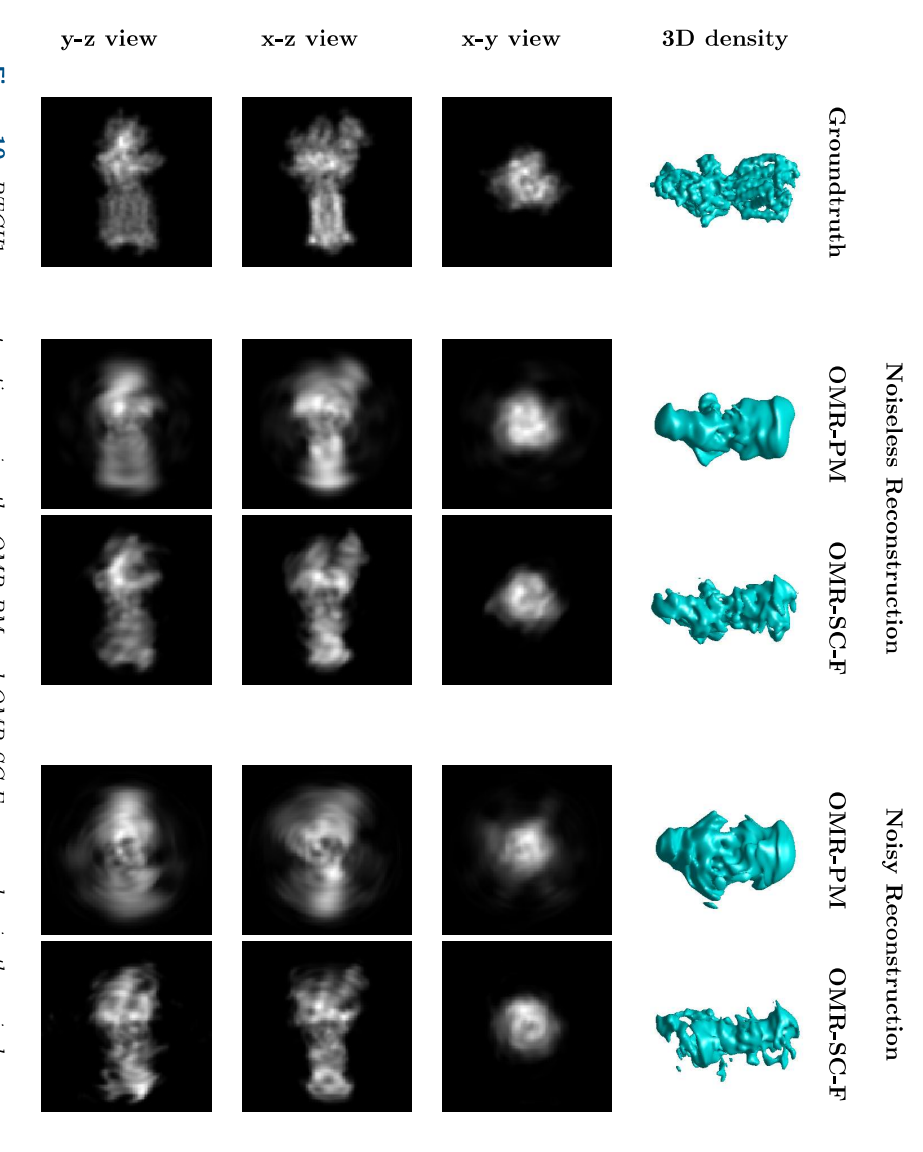
spherical harmonic degrees. A naive attempt to use off-the-shelf (or even bespoke) denoisers tion images to counter the noise and extract features of sufficient quality, especially at high The main drawback of the proposed OMR-SC is that it needs a large number of projec-



the noisy case (SNR = 0.1). Figure 9. HJC: reconstructions using the OMR-PM and OMR-SC-F approaches in the noiseless case and

computational complexity grow exponentially with the moment order. higher-order moments is challenging since, for a fixed SNR, noise amplification and the related images. Further, like prior work, OMR-SC relies on first- and second-order moments. tant challenge to design schemes that simultaneously extract features and denoise projection could improve the situation by denoising the extracted features, it is an interesting and imporduce typically unknown bias which makes them unsuitable for feature extraction. While we fails; since current image denoising methods only aim to improve image quality, they intro-

ments used in our approach remains an open question. number of initialization (≈ 10) suffices to obtain a good reconstruction. Alas, unlike for phase multiple initializations can be carried out in parallel, and we empirically found that a small tialization in phase retrieval with random measurements. Importantly, the reconstructions for challenge: a data-dependent, efficiently computable initialization reminiscent of spectral ini-We proposed an effective computational strategy that greatly reduces the impact of this retrieval with random measurements, existence of theoretical guarantees for deterministic mo-Another major challenge is the nonconvexity introduced by the orthogonality constraints



and the noisy case (SNR = 0.1). Figure 10. PTCH1: reconstructions using the OMR-PM and OMR-SC-F approaches in the noiseless case

Table 8

Resolutions (Å) and correlation coefficients of recovered protein density maps using the OMR-SC-F approaches with the random (R) and proposed (P) initialization schemes (FSC cutoff threshold = 0.5). Noisy Noiseless OMR-SC-F (R) OMR-SC-F (P) OMR-SC-F (R) OMR-SC-F (P) 31.7814.04CaS15.99Resolution (Å) 41.8829.3826.12HJC28.20 31.38 16.5230.00PTCH1 0.75 **0.87** 0.930.85CaS Correlation coefficient 0.61 **0.73** 0.78HJC0.780.860.740.71 PTCH1

16.15

36.82

of size $G \times G$, and the noisy image $S(x,y) = P(x,y) + \epsilon(x,y)$. We compute the frequency component $\widehat{S}(k_x,k_y)$ using the discrete (nonuniform) Fourier transform Appendix A. Noisy feature debiasing. Let P(x,y) denote the noiseless projection image

Resolutions (Å) and correlation coefficients of recovered protein density maps using the OMR-SC-F approaches with (w/) and without (w/o) nonnegativity constraints (FSC cutoff threshold = 0.5).

Noiseless (OMR-SC-F (w/o) OMR-SC-F (w) OMR-SC-F (w/o)	CaS 14.23 14.04 17.11	Resolution (Å) HJC PT 39.62 24. 29.38 16 72.89 32.	(Å) PTCH1 24.27 16.52 32.68		Correlation coefficient CaS HJC PTCH 0.92 0.67 0.77 0.93 0.78 0.86 0.85 0.58 0.77
		14.23 14.04	39.62 29.38	24.27 16.52	0.0	
νI)MR-SC-F (w/o)		72.89	32.68	, al	- 1

$$\begin{split} \widehat{S}(k_x, k_y) &= \sum_{x} \sum_{y} \exp\left(-\mathbf{i} \cdot [k_x \ k_y] \left[\begin{array}{c} x \\ y \end{array}\right]\right) \cdot \left(P(x, y) + \epsilon(x, y) \right) \\ &= f_k^T(p + \epsilon), \end{split}$$

the vectorized exponential term to compute $\tilde{S}(k)$. where p is the vectorized projection image P(x,y), ϵ is the vectorized noise $\epsilon(x,y)$, and f_k is

images in (2.8) can thus be replaced by an expectation operator. The bias term $\zeta(k_1, k_2, \psi)$ converges almost surely to the expected value. Fourier autocorrelation feature. When the number of projection images goes to i.e., $N \to \infty$, according to the strong law of large numbers, the sample average s almost surely to the expected value. The average with respect to the projection

$$\zeta(k_1, k_2, \psi) = \mathbb{E}\left[\frac{1}{2\pi} \int_0^{2\pi} \boldsymbol{f}_{\boldsymbol{k}_1}^T(\boldsymbol{p} + \boldsymbol{\epsilon}) \cdot \boldsymbol{f}_{\boldsymbol{k}_2}^* T(\boldsymbol{p} + \boldsymbol{\epsilon}) \ d\varphi_{\boldsymbol{k}_1}\right]
- \mathbb{E}\left[\frac{1}{2\pi} \int_0^{2\pi} \boldsymbol{f}_{\boldsymbol{k}_1}^T \boldsymbol{p} \cdot \boldsymbol{f}_{\boldsymbol{k}_2}^* T \boldsymbol{p} \ d\varphi_{\boldsymbol{k}_1}\right],$$

where $\varphi_{k_1} = \measuredangle k_1$ and $\varphi_{k_1} + \psi = \measuredangle \kappa_2$. The house κ_n is independent from the projection image p and $\mathbb{E}[\epsilon] = 0$, we have $= \angle \mathbf{k}_1$ and $\varphi_{\mathbf{k}_1} + \psi = \angle \mathbf{k}_2$. The noise ϵ_n is modeled as AWGN with variance σ_{ϵ}^2 [6]

$$\mathbb{E}\left[\frac{1}{2\pi}\int_{0}^{2\pi}\widehat{\rho}(\mathbf{k}_{1})\cdot\widehat{\rho}^{*}(\mathbf{k}_{2})\ d\varphi_{\mathbf{k}_{1}}\right]$$

$$=\frac{1}{2\pi}\int_{0}^{2\pi}\mathbb{E}\left[f_{\mathbf{k}_{1}}^{T}\mathbf{p}\cdot f_{\mathbf{k}_{2}}^{*}^{T}\mathbf{p}\right]\ d\varphi_{\mathbf{k}_{1}}+\frac{1}{2\pi}\int_{0}^{2\pi}\mathbb{E}\left[f_{\mathbf{k}_{1}}^{T}\mathbf{p}\cdot f_{\mathbf{k}_{2}}^{*}^{T}\mathbf{\epsilon}\right]\ d\varphi_{\mathbf{k}_{1}}$$

$$+\frac{1}{2\pi}\int_{0}^{2\pi}\mathbb{E}\left[f_{\mathbf{k}_{1}}^{T}\mathbf{p}\cdot f_{\mathbf{k}_{2}}^{*}^{T}\mathbf{p}\right]\ d\varphi_{\mathbf{k}_{1}}+\frac{1}{2\pi}\int_{0}^{2\pi}\mathbb{E}\left[f_{\mathbf{k}_{1}}^{T}\mathbf{p}\cdot f_{\mathbf{k}_{2}}^{*}^{T}\mathbf{\epsilon}\right]\ d\varphi_{\mathbf{k}_{1}}$$

$$=\frac{1}{2\pi}\int_{0}^{2\pi}\mathbb{E}\left[f_{\mathbf{k}_{1}}^{T}\mathbf{p}\cdot f_{\mathbf{k}_{2}}^{*}\mathbb{E}[\mathbf{p}]\ d\varphi_{\mathbf{k}_{1}}+\frac{1}{2\pi}\int_{0}^{2\pi}\mathbb{E}\left[f_{\mathbf{k}_{1}}^{T}\mathbf{\epsilon}\cdot f_{\mathbf{k}_{2}}^{*}\mathbb{E}[\mathbf{\epsilon}]\ d\varphi_{\mathbf{k}_{1}}$$

$$=\frac{1}{2\pi}\int_{0}^{2\pi}\mathbb{E}\left[f_{\mathbf{k}_{1}}^{T}\mathbf{p}\cdot f_{\mathbf{k}_{2}}^{*}\mathbb{E}[\mathbf{p}]\ d\varphi_{\mathbf{k}_{1}}+\frac{1}{2\pi}\int_{0}^{2\pi}\mathbb{E}\left[f_{\mathbf{k}_{1}}^{T}\mathbf{\epsilon}\cdot f_{\mathbf{k}_{2}}^{*}^{T}\mathbf{\epsilon}\right]\ d\varphi_{\mathbf{k}_{1}}$$

$$=\frac{1}{2\pi}\int_{0}^{2\pi}\mathbb{E}\left[f_{\mathbf{k}_{1}}^{T}\mathbf{p}\cdot f_{\mathbf{k}_{2}}^{*}\mathbb{E}\left[f_{\mathbf{k}_{1}}^{T}\mathbf{p}\cdot f_{\mathbf{k}_{2}}^{*}\right]\right]$$

1428

From the above (A.3), we can get the following bias term:

$$\frac{1}{2\pi} \int_{0}^{2\pi} \mathbb{E}\left[f_{\mathbf{k}_{1}}^{T} \epsilon \cdot f_{\mathbf{k}_{2}}^{*}^{T} \epsilon\right] d\varphi_{\mathbf{k}_{1}}
= \frac{1}{2\pi} \int_{0}^{2\pi} \mathbb{E}\left[\left(\sum_{i} f_{\mathbf{k}_{1}}(i) \cdot \epsilon_{i}\right) \cdot \left(\sum_{j} f_{\mathbf{k}_{2}}^{*}(j) \cdot \epsilon_{j}\right)\right] d\varphi_{\mathbf{k}_{1}}
= \frac{1}{2\pi} \int_{0}^{2\pi} \mathbb{E}\left[\sum_{i} f_{\mathbf{k}_{1}}(i) f_{\mathbf{k}_{2}}^{*}(i) \cdot \epsilon_{i}^{2} + \sum_{i \neq j} f_{\mathbf{k}_{1}}(i) f_{\mathbf{k}_{2}}^{*}(j) \cdot \epsilon_{i} \epsilon_{j}\right] d\varphi_{\mathbf{k}_{1}}
= \frac{1}{2\pi} \int_{0}^{2\pi} \sum_{i} f_{\mathbf{k}_{1}}(i) f_{\mathbf{k}_{2}}^{*}(i) \cdot \mathbb{E}\left[\epsilon_{i}^{2}\right] + \sum_{i \neq j} f_{\mathbf{k}_{1}}(i) f_{\mathbf{k}_{2}}^{*}(j) \cdot \mathbb{E}\left[\epsilon_{i} \epsilon_{j}\right] d\varphi_{\mathbf{k}_{1}}
= \mathbb{E}\left[\epsilon^{2}\right] \cdot \sum_{i} \sum_{j} \frac{1}{2\pi} \int_{0}^{2\pi} \exp\left(-\mathbf{i} \cdot (\mathbf{k}_{1} - \mathbf{k}_{2})^{T} \begin{bmatrix} x \\ y \end{bmatrix}\right) d\varphi_{\mathbf{k}_{1}}.$$

$$(4)$$

Since the noise ϵ is additive white Gaussian with variance σ_{ϵ}^2 , we have that $\mathbb{E}[\epsilon^2] = \sigma_{\epsilon}^2$. The bias term of the autocorrelation function is then

(A.5)
$$\zeta(k_1, k_2, \psi) = \sigma_{\epsilon}^2 \cdot \sum_{x} \sum_{y} \frac{1}{2\pi} \int_{0}^{2\pi} \exp\left(-\mathbf{i} \cdot (\mathbf{k}_1 - \mathbf{k}_2)^T \begin{bmatrix} x \\ y \end{bmatrix}\right) d\varphi_{k_1}.$$

A.2. Fourier radial feature. When the number of projections images goes to infinity, the average with respect to the projection images in (3.1) can also be replaced by the expectation

$$\mathbb{E}\left[\frac{1}{2\pi} \int_{0}^{2\pi} \widehat{\rho}(\mathbf{k}) \ d\varphi_{\mathbf{k}}\right] = \frac{1}{2\pi} \int_{0}^{2\pi} \mathbb{E}\left[f_{\mathbf{k}}^{T}(\mathbf{p} + \boldsymbol{\epsilon})\right] \ d\varphi_{\mathbf{k}}$$

$$= \frac{1}{2\pi} \int_{0}^{2\pi} \mathbb{E}\left[f_{\mathbf{k}}^{T}\mathbf{p}\right] \ d\varphi_{\mathbf{k}} + \frac{1}{2\pi} \int_{0}^{2\pi} \sum_{i} f_{\mathbf{k}}(i) \mathbb{E}\left[\epsilon\right] \ d\varphi_{\mathbf{k}}$$

$$= \frac{1}{2\pi} \int_{0}^{2\pi} \mathbb{E}\left[f_{\mathbf{k}}^{T}\mathbf{p}\right] \ d\varphi_{\mathbf{k}}.$$

We can see that we do not need to perform debiasing on M(k) since $\mathbb{E}[\epsilon] = 0$

autocorrelation feature $E_l(r_1, r_2)$ can be rewritten as Appendix B. Autocorrelation function in the spatial domain. Using (3.5), the spatial

ORTHOGONAL MATRIX RETRIEVAL WITH SPATIAL CONSENSUS

$$E_{l}(r_{1}, r_{2}) = \sum_{m=-l}^{l} B_{lm}(r_{1}) \cdot B_{lm}(r_{2})$$

$$= \frac{1}{r_{1}^{2} r_{2}^{2}} \iiint \iiint \rho(\tilde{r}_{1}) \cdot \delta(r_{1} - \tilde{r}_{1}) \cdot \rho(\tilde{r}_{2}) \cdot \delta(r_{2} - \tilde{r}_{2})$$

$$\times \sum_{m=-l}^{l} Y_{lm}(\theta_{\tilde{r}_{1}}, \varphi_{\tilde{r}_{1}}) \cdot Y_{lm}(\theta_{\tilde{r}_{2}}, \varphi_{\tilde{r}_{2}}) d\tilde{r}_{1} d\tilde{r}_{2}$$

$$= \frac{1}{r_{1}^{2} r_{2}^{2}} \iiint \iiint \rho(\tilde{r}_{1}) \cdot \delta(r_{1} - \tilde{r}_{1}) \cdot \rho(r_{2}) \cdot \delta(r_{2} - \tilde{r}_{2})$$

$$\times \frac{2l+1}{4\pi} P_{l}(\cos \psi_{\tilde{r}_{1}}, \tilde{r}_{2}) d\tilde{r}_{1} d\tilde{r}_{2},$$

where $\psi_{\tilde{r}_1,\tilde{r}_2}$ is the angle between \tilde{r}_1 and \tilde{r}_2 . The autocorrelation function $E(r_1,r_2,\psi)$ can be computed from $E_l(r_1,r_2)$ using the completeness of Legendre polynomials as follows:

$$E(r_{1}, r_{2}, \psi) = \sum_{l=0}^{\infty} E_{l}(r_{1}, r_{2}) \cdot P_{l}(\cos \psi)$$

$$= \frac{1}{r_{1}^{2}r_{2}^{2}} \iiint \iiint \rho(\tilde{r}_{1}) \cdot \delta(r_{1} - \tilde{r}_{1}) \cdot \rho(\tilde{r}_{2}) \cdot \delta(r_{2} - \tilde{r}_{2})$$

$$\times \frac{1}{2\pi} \sum_{l=0}^{\infty} \frac{2l+1}{2} P_{l}(\cos \psi_{\tilde{r}_{1}, \tilde{r}_{2}}) \cdot P_{l}(\cos \psi) d\tilde{r}_{1} d\tilde{r}_{2}$$

$$= \frac{1}{r_{1}^{2}r_{2}^{2}} \iiint \iiint \rho(\tilde{r}_{1}) \cdot \delta(r_{1} - \tilde{r}_{1}) \cdot \rho(\tilde{r}_{2}) \cdot \delta(r_{2} - \tilde{r}_{2})$$

$$\times \frac{1}{2\pi} \cdot \delta(\cos \psi_{\tilde{r}_{1}, \tilde{r}_{2}} - \cos \psi) d\tilde{r}_{1} d\tilde{r}_{2}$$

$$= \frac{1}{2\pi r_{1}^{2}r_{2}^{2}} \iiint \iiint \rho(\tilde{r}_{1}) \cdot \delta(r_{1} - \tilde{r}_{1}) \cdot \rho(\tilde{r}_{2}) \cdot \delta(r_{2} - \tilde{r}_{2})$$

$$\times \delta(\psi_{\tilde{r}_{1}, \tilde{r}_{2}} - \psi) d\tilde{r}_{1} d\tilde{r}_{2},$$

where $\psi \in [0, \pi]$.

ian basis function at the sampling location μ_d is Appendix C. Spherical harmonic expansion of the Gaussian basis function. The Gauss-

$$h(\boldsymbol{r}-\boldsymbol{\mu}_d) = \frac{1}{(2\pi)^{\frac{3}{2}}\sigma^3} \exp\left(-\frac{1}{2}\frac{\|\boldsymbol{r}-\boldsymbol{\mu}_d\|_2^2}{\sigma^2}\right).$$

It can be expanded in real spherical harmonics

$$h(\mathbf{r} - \boldsymbol{\mu}_d) = \sum_{l=0}^{\infty} \sum_{m=-l}^{l} g_{lm}(r, \boldsymbol{\mu}_d) \cdot Y_{lm}(\theta_{\boldsymbol{r}}, \varphi_{\boldsymbol{r}}),$$

 $g_{lm}(r, \mu_d)$ is the expansion coefficient, where $Y_{lm}(\theta_r, \varphi_r)$ is the real spherical harmonic function of degree l and order

$$(C.3) \qquad g_{lm}(r,\boldsymbol{\mu}_d) = \int_0^{2\pi} \int_0^{\pi} h(\boldsymbol{r} - \boldsymbol{\mu}_d) \cdot Y_{lm}(\theta_{\boldsymbol{r}},\varphi_{\boldsymbol{r}}) \ d\theta_{\boldsymbol{r}} d\varphi_{\boldsymbol{r}}$$

$$= \frac{1}{(2\pi)^{\frac{3}{2}} \sigma^3} \exp\left(-\frac{1}{2} \frac{r^2 + \|\boldsymbol{\mu}_d\|_2^2}{\sigma^2}\right) \int_0^{2\pi} \int_0^{\pi} \exp\left(\frac{\boldsymbol{r}^T \boldsymbol{\mu}_d}{\sigma^2}\right) \cdot Y_{lm}(\theta_{\boldsymbol{r}},\varphi_{\boldsymbol{r}}) \sin\theta_{\boldsymbol{r}} d\theta_{\boldsymbol{r}} d\varphi_{\boldsymbol{r}}$$

(1) When $\mu_d = 0$, we have

(C.4)
$$h(\mathbf{r} - \mathbf{0}) = \left(\frac{1}{(2\pi)^{\frac{3}{2}}\sigma^3} \exp\left(-\frac{1}{2}\frac{r^2}{\sigma^2}\right)\sqrt{4\pi}\right) \cdot \sqrt{\frac{1}{4\pi}}$$
$$= g_{00}(r, \mathbf{0}) \cdot Y_{00}(\theta_{\mu_d}, \varphi_{\mu_d}),$$

where $Y_{00}(\theta_{\mu_d}, \varphi_{\mu_d}) = \sqrt{\frac{1}{4\pi}}$. (2) When $\mu_d \neq 0$, we can use the Funk–Hecke formula and get

$$\begin{aligned} & \int_{0}^{2\pi} \int_{0}^{\pi} \exp\left(\frac{r^{T} \boldsymbol{\mu}_{d}}{\sigma^{2}}\right) \cdot Y_{lm}(\theta_{\boldsymbol{r}}, \varphi_{\boldsymbol{r}}) \sin \theta_{\boldsymbol{r}} \ d\theta_{\boldsymbol{r}} d\varphi_{\boldsymbol{r}} \\ &= \frac{4\pi \cdot c_{l}(r, \|\boldsymbol{\mu}_{d}\|_{2})}{2l+1} \cdot Y_{lm}(\theta_{\boldsymbol{\mu}_{d}}, \varphi_{\boldsymbol{\mu}_{d}}), \end{aligned}$$

denote the angle between r and μ_d , and $\kappa = \cos \psi_{r,\mu_d}$. We can compute $c_l(r, \|\mu_d\|_2)$ where $c_l(r, \|\boldsymbol{\mu}_d\|_2)$ is the Legendre series expansion coefficient of $\exp\left(\frac{r^T \mu_d}{\sigma^2}\right)$. Let ψ_{r, μ_d}

(C.6)
$$c_{l}(r, \|\boldsymbol{\mu}_{d}\|_{2}) = \frac{2l+1}{2} \int_{-1}^{1} \exp\left(\frac{r\|\boldsymbol{\mu}_{d}\|_{2} \cdot \kappa}{\sigma^{2}}\right) \cdot P_{l}(\kappa) d\kappa$$
$$= \sqrt{\frac{\pi}{2r\|\boldsymbol{\mu}_{d}\|_{2}}} \cdot \sigma \cdot (2l+1) \cdot I_{l+\frac{1}{2}} \left(\frac{r\|\boldsymbol{\mu}_{d}\|_{2}}{\sigma^{2}}\right),$$

function $\hat{I}_{\nu}(\cdot)$ instead: where $P_l(\cdot)$ is the Legendre polynomial and $I_{\nu}(\cdot)$ is the modified Bessel function of the first kind of order ν . To avoid numeric overflow, we often use the scaled Bessel

$$\widehat{I}_{l+\frac{1}{2}} \left(\frac{r \|\boldsymbol{\mu}_d\|_2}{\sigma^2} \right) = \exp\left(-\frac{r \|\boldsymbol{\mu}_d\|_2}{\sigma^2} \right) \cdot I_{l+\frac{1}{2}} \left(\frac{r \|\boldsymbol{\mu}_d\|_2}{\sigma^2} \right).$$

The expansion coefficient $g_{lm}(r, \mu_d)$ is then

(C.8)
$$g_{lm}(r, \boldsymbol{\mu}_d) = \frac{1}{\sigma^2} \exp\left(-\frac{1}{2} \frac{(r - ||\boldsymbol{\mu}_d||_2)^2}{\sigma^2}\right) \sqrt{\frac{1}{r||\boldsymbol{\mu}_d||_2}} \cdot \widehat{l}_{l+\frac{1}{2}} \left(\frac{r||\boldsymbol{\mu}_d||_2}{\sigma^2}\right) \times Y_{lm}(\theta_{\boldsymbol{\mu}_d}, \varphi_{\boldsymbol{\mu}_d}).$$

Appendix D. Linear formulation of spatial radial features. We first give the detailed

$$M(k) = \frac{1}{N} \sum_{n=1}^{N} \frac{1}{2\pi} \int_{0}^{2\pi} \widehat{S}_{n}(\mathbf{k}) d\varphi$$

$$N \stackrel{\sim}{=} \infty \frac{\int_{0}^{2\pi} \int_{0}^{\pi} \widehat{\rho}(\mathbf{k}) \cdot k^{2} \sin \theta_{\mathbf{k}} d\varphi_{\mathbf{k}} d\theta_{\mathbf{k}}}{\int_{0}^{2\pi} \int_{0}^{\pi} k^{2} \sin \theta_{\mathbf{k}} d\varphi_{\mathbf{k}} d\theta_{\mathbf{k}}}$$

$$= \iiint \frac{\int_{0}^{2\pi} \int_{0}^{\pi} e^{-i\mathbf{k} \cdot \mathbf{r}} k^{2} \sin \theta_{\mathbf{k}} d\theta_{\mathbf{k}} d\varphi_{\mathbf{k}}}{\int_{0}^{2\pi} \int_{0}^{\pi} k^{2} \sin \theta_{\mathbf{k}} d\varphi_{\mathbf{k}} d\theta_{\mathbf{k}}} \cdot \rho(\mathbf{r}) d\mathbf{r}$$

$$= \iiint \frac{\int_{0}^{2\pi} d\varphi_{\mathbf{k}, \mathbf{r}} \int_{0}^{\pi} e^{-ik\mathbf{r} \cos \theta_{\mathbf{k}, \mathbf{r}} k^{2} \sin \theta_{\mathbf{k}, \mathbf{r}}} d\theta_{\mathbf{k}, \mathbf{r}}}{\int_{0}^{2\pi} d\varphi_{\mathbf{k}, \mathbf{r}} \int_{0}^{\pi} k^{2} \sin \theta_{\mathbf{k}, \mathbf{r}}} d\theta_{\mathbf{k}, \mathbf{r}}$$

$$= \iiint \frac{\sin(k\mathbf{r})}{k\mathbf{r}} \cdot \rho(\mathbf{r}) d\mathbf{r},$$

where φ is the azimuth angle of k in the Fourier slice \widehat{S}_n and $(\theta_{k,r}, \varphi_{k,r})$ is the angular direction of k with respect to r when r was selected as the pseudo-z-axis during a change of

As derived in (4.5), we can compute the radial feature W(r) as

$$W(r) = \iiint_{d=1}^{D} \rho(\tilde{r})\delta(r - \tilde{r}) d\tilde{r}$$

$$= \sum_{d=1}^{D} w_d \cdot \iiint_{(2\pi)^{\frac{3}{2}}\sigma^3} \exp\left(-\frac{1}{2} \frac{\|\tilde{r} - \boldsymbol{\mu}_d\|_2^2}{\sigma^2}\right) \cdot \delta(r - \tilde{r}) d\tilde{r}$$

$$= \sum_{d=1}^{D} w_d \cdot \frac{1}{(2\pi)^{\frac{3}{2}}\sigma^3} \int \exp\left(-\frac{1}{2} \frac{\tilde{r}^2 + \|\boldsymbol{\mu}_d\|_2^2}{\sigma^2}\right)$$

$$\times \left(\int_0^{2\pi} \int_0^{\pi} \exp\left(\frac{\tilde{r}^T \boldsymbol{\mu}_d}{\sigma^2}\right) \sin\theta_{\tilde{r}} d\theta_{\tilde{r}} d\varphi_{\tilde{r}}\right) \cdot \tilde{r}^2 \cdot \delta(r - \tilde{r}) d\tilde{r},$$
which can be simplified as

which can be simplified as

ch can be simplified as
$$W(r) = \sum_{d=1}^{D} w_d \cdot g(r, \boldsymbol{\mu}_d).$$
(1) When $r=0$, we have
$$g(r, \boldsymbol{\mu}_d) = \frac{1}{(2\pi)^{\frac{3}{2}}\sigma^3} \exp\left(-\frac{1}{2} \frac{\|\boldsymbol{\mu}_d\|_2^2}{\sigma^2}\right).$$

(2) When $r \neq 0$ and $||\boldsymbol{\mu}_d||_2 = 0$, we have

$$(\mathrm{D.4}) \qquad \qquad g(r, \boldsymbol{\mu}_d) = 4\pi r^2 \cdot \frac{1}{(2\pi)^{\frac{3}{2}}\sigma^3} \exp\left(-\frac{1}{2}\frac{r^2}{\sigma^2}\right).$$

When $r \neq 0$ and $\|\boldsymbol{\mu}_d\|_2 \neq 0$, by using (C.5), (C.6) and setting l = 0, m = 0, we can

$$(D.5) \qquad \int_{0}^{2\pi} \int_{0}^{\pi} \exp\left(\frac{\tilde{r}^{T} \mu_{d}}{\sigma^{2}}\right) \sin\theta_{\tilde{r}} \ d\theta_{\tilde{r}} d\varphi_{\tilde{r}} = 4\pi \cdot \sqrt{\frac{\pi}{2r \|\mu_{d}\|_{2}}} \cdot \sigma \cdot I_{\frac{1}{2}} \left(\frac{r \|\mu_{d}\|_{2}}{\sigma^{2}}\right)$$

$$Plugging (D.5) \text{ into (D.1), and using the scaled Bessel function in (C.7), we have}$$

$$(D.6) \qquad g(r, \mu_{d}) = \frac{r^{2}}{\sigma^{2}} \exp\left(-\frac{1}{2} \frac{(r - \|\mu_{d}\|_{2})^{2}}{\sigma^{2}}\right) \sqrt{\frac{1}{r \|\mu_{d}\|_{2}}} \cdot \hat{I}_{\frac{1}{2}} \left(\frac{r \|\mu_{d}\|_{2}}{\sigma^{2}}\right).$$

$$(\mathrm{D.6}) \qquad \qquad g(r, \pmb{\mu}_d) = \frac{r^2}{\sigma^2} \exp\left(-\frac{1}{2} \frac{(r - \|\pmb{\mu}_d\|_2)^2}{\sigma^2}\right) \sqrt{\frac{1}{r \|\pmb{\mu}_d\|_2} \cdot \widehat{I}_{\frac{1}{2}}} \left(\frac{r}{2}\right)^2}$$

We then have the following measurement vector $\boldsymbol{g}(r)$

$$\mathbf{g}(r) = [g(r, \boldsymbol{\mu}_1) \quad g(r, \boldsymbol{\mu}_2) \quad \cdots \quad g(r, \boldsymbol{\mu}_D)]^T.$$

Appendix E. Quadratic formulation of spatial autocorrelation features. As derived in (3.6) of section 3.2, the autocorrelation feature $E_l(r_1, r_2)$ is given by

(3.6) of section 3.2, the autocorrelation feature
$$E_l(r_1, r_2)$$
 is given by
$$E_l(r_1, r_2) = \sum_{m=-l}^{l} \iiint \rho(\tilde{r}_1) \cdot \delta(r_1 - \tilde{r}_1) \cdot Y_{lm}(\theta_{\tilde{r}_1}, \varphi_{\tilde{r}_1}) \sin \theta_{\tilde{r}_1} \ d\tilde{r}_1 d\theta_{\tilde{r}_1} d\varphi_{\tilde{r}_1}$$

$$\times \iiint \rho(\tilde{r}_2) \cdot \delta(r_2 - \tilde{r}_2) \cdot Y_{lm}(\theta_{\tilde{r}_2}, \varphi_{\tilde{r}_2}) \sin \theta_{\tilde{r}_2} \ d\tilde{r}_2 d\theta_{\tilde{r}_2} \varphi_{\tilde{r}_2}.$$

$$(E.1) \qquad E_{l}(r_{1},r_{2}) = \sum_{m=-l} \iiint \rho(\tilde{r}_{1}) \cdot \delta(r_{1} - \tilde{r}_{1}) \cdot Y_{lm}(\theta_{\tilde{r}_{1}},\varphi_{\tilde{r}_{1}}) \sin\theta_{\tilde{r}_{1}} d\tilde{r}_{1} d\theta_{\tilde{r}_{1}} d\varphi_{\tilde{r}_{1}} \\ \times \iiint \rho(\tilde{r}_{2}) \cdot \delta(r_{2} - \tilde{r}_{2}) \cdot Y_{lm}(\theta_{\tilde{r}_{2}},\varphi_{\tilde{r}_{2}}) \sin\theta_{\tilde{r}_{3}} d\tilde{r}_{2} d\theta_{\tilde{r}_{3}} \varphi_{\tilde{r}_{2}}. \\ \text{Using } (4.4), \text{ we can compute the following integration:} \\ B_{l}^{m}(r) = \iiint \rho(\tilde{r}) \cdot \delta(r - \tilde{r}) \cdot Y_{lm}(\theta_{\tilde{r}},\varphi_{\tilde{r}}) \sin\theta_{\tilde{r}} d\tilde{r} d\theta_{\tilde{r}} d\varphi_{\tilde{r}} \\ = \sum_{d=1}^{D} w_{d} \cdot \sum_{l'=0}^{\infty} \sum_{m'=-l'} g_{l'm'}(r,\mu_{d}) \cdot \iint Y_{l'm'}(\theta_{\tilde{r}},\varphi_{\tilde{r}}) \cdot Y_{lm}(\theta_{\tilde{r}},\varphi_{\tilde{r}}) \sin\theta_{\tilde{r}} d\theta_{\tilde{r}} d\varphi_{\tilde{r}} \\ = \sum_{d=1}^{D} w_{d} \cdot \sum_{l'=0}^{\infty} \sum_{m'=-l'} g_{l'm'}(r,\mu_{d}) \cdot \delta(l'=l) \delta(m'=m) \\ = \sum_{d=1}^{D} w_{d} \cdot g_{lm}(r,\mu_{d}) \\ = \sum_{d=1}^{D} w_{d} \cdot g_{lm}(r,\mu_{d})$$

Using (E.2), we can get the quadratic formulation of $E_l(r_1, r_2)$:

$$egin{aligned} egin{aligned} & egin{$$

where $\boldsymbol{w} = [w_1, \dots, w_D]^T$ and the real measurement vector $\boldsymbol{g}_{lm}(r)$ is

(E.3)
$$g_{lm}(r) = [g_{lm}(r, \mu_1) \quad g_{lm}(r, \mu_2) \quad \cdots \quad g_{lm}(r, \mu_D)]^T$$

computational complexities: and G. The proposed OMR-SC approach consists of the following three steps with different linearly with G, i.e., $\mathcal{O}(G)$. For simplification, we shall give the complexity in terms of L, N, size of the projection image is $G \times G$. In general, the number of sampled points Φ, V, U scales denote the spherical harmonic bandwidth. There are a total of N projection images, dimension of r, U denote the number of sampling points along the dimension of k, and Lpoints along the dimension of φ , V denote the number of selected GLQ points along the Appendix F. Computational complexity. Let Φ denote the number of selected GLQ

- (1) Feature extraction. is $\mathcal{O}(NG^2 \log G)$. The complexity of calculating $\{M(k)\}_k$ is $\mathcal{O}(NU\Phi) = \mathcal{O}(NG^2)$. The complexity of calculating $\{W(r)\}_r$ is $\mathcal{O}(VU) = \mathcal{O}(G^2)$. The overall complexity of calculating $\{C_l(k_1, k_2)\}_l$ from $\widetilde{C}_{\mathrm{FB}}$ is $\mathcal{O}(LG^3)$. The complexity of performing Cholesky decompositions of $\{C_l\}_l$ is $\mathcal{O}(LU^3) = \mathcal{O}(LG^3)$. The overall complexity of extracting the Fourier autocorrelation features is $\mathcal{O}(NG^3 + LG^3) = \mathcal{O}(NG^3 + LG^3)$. The $\mathcal{O}\left(NG^3 + LG^3\right)$ The overall complexity of feature extraction is as $\mathcal{O}\left(NG^3 + L\dot{G}^3 + NG^2\log G\right)$ extracting the spatial radial features is $\mathcal{O}\left(NG^2\log G + NG^2 + G^2\right) = \mathcal{O}\left(NG^2\log G\right)$. complexity of calculating the nonuniform FFT $\{\hat{S}_n(k,\varphi)\}_n$ from N projection images of $C(k_1, k_2, \psi)$ using the fast steerable PCA and CWF is $\mathcal{O}(NG^3)$. The complexity of The complexity of computing the Fourier–Bessel expansion C_{FB}
- (2) Optimization of $\{O_l\}_{l=1}^L$. The complexity of computing $\{B_l^T(w)Q_lF_l\}_l$ is $\mathcal{O}(L^2(LVL+VUL)) = \mathcal{O}(L^3(LV+VU)) = \mathcal{O}(L^3(LG+G^2))$. The complexity of performing singular value decomposition of $\{B_l(z)^*Q_lF_l\}_l$ is $\mathcal{O}(L^4)$. The complexity of com- $\mathcal{O}(L^3(LG+G^2)).$ puting $\{V_l U_l^T\}_l$ is $\mathcal{O}(L^4)$. The overall complexity of computing $\{O_l\}_{l=1}^L$ is thus
- \odot Optimization of w. The complexity of computing the vector $b_l(r, w)$ is $\mathcal{O}(lr^2)$. Since Vprojection operation $\mathcal{P}_{\mathcal{S}}(\cdot)$ has a compl of computing w is $\mathcal{O}(L^2G^3+G^3\log G)$. is $\mathcal{O}(G^3)$. The complexity of computing the gradient $\nabla f_2(\boldsymbol{w})$ is $\mathcal{O}(L^2G^3)$, and the projection operation $\mathcal{P}_S(\cdot)$ has a complexity of $\mathcal{O}(G^3 \log G)$. The overall complexity a radial feature $g(v)^T w$ is $\mathcal{O}(r^2)$, and the complexity of evaluating all radial features of computing $\{B_l(\boldsymbol{w})\}_l$ is then $\mathcal{O}(L^2G^3)$. Computing $\{A_l\}_l$ via (3.19) only increases the complexity of evaluating features to $\mathcal{O}(L^2G^3+L^2G^2)$. The complexity of evaluating and G are typically in the same order as G, i.e., $\mathcal{O}(V) = \mathcal{O}(U) = \mathcal{O}(G)$, the complexity

for any orthogonal O_l of size $(2l+1) \times (2l+1)$, that **Appendix G. OMR-SC-S.** For the spatial autocorrelation feature matrix E_l , we have

$$(3.1) E_l = B_l O_l^T O_l B_l^T = P_l P_l^T,$$

where $P_l = B_l O_l^T$ OMR-SC-S is then $m{B}_l m{O}_l^T$ is obtained via the Cholesky decomposition of E_l . The formulation of

fashion as in section 5.1. As summarized in Algorithm G.1, we can compute $\{O_l\}_{l=1}^L$ and \boldsymbol{w} in a similar alternating

the errors from the lower spherical harmonic degrees when Fourier autocorrelations are used. concentrated in the first few degrees. As a result, OMR-SC puts more effort into minimizing harmonic expansion coefficients, and the energy of Fourier expansion coefficients is mostly coefficients is more evenly distributed across different degrees than that of Fourier spherical "D1," for example; as shown in Figure 11, the energy of spatial spherical harmonic expansion for the performance differences, we take a closer look at the two features. Take the density Tables 1 and 2, OMR-SC-F performs better than OMR-SC-S. To find out possible causes Performance comparison of spatial and Fourier autocorrelations. As shown in

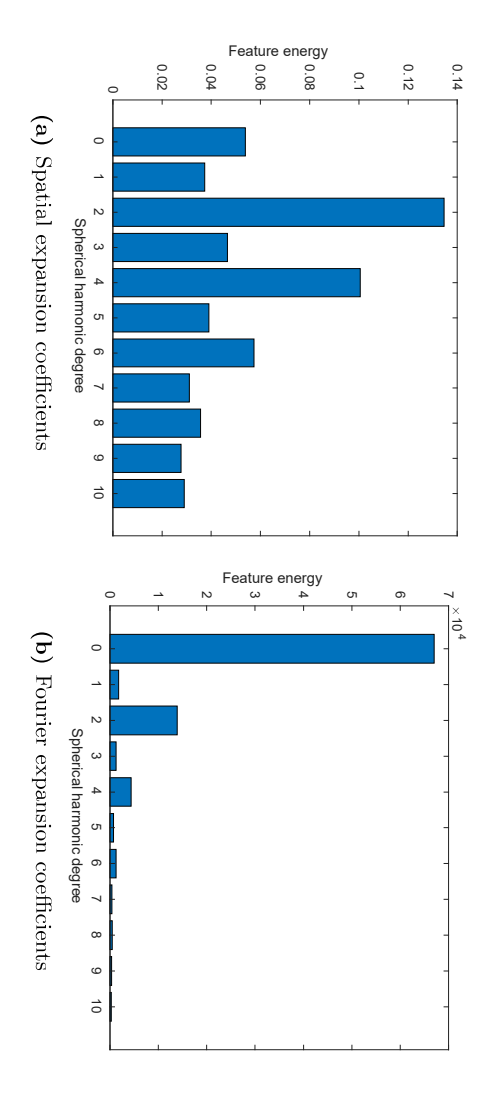


Figure 11. Energy distributions of spatial and Fourier spherical harmonic expansion coefficients

Algorithm G.1. OMR-SC-S

ORTHOGONAL MATRIX RETRIEVAL WITH SPATIAL CONSENSUS

Require: threshold ς . Denoised reference projections $\{\overline{S}_i \mid h=1,\ldots,H\}$, step size η , convergence

- Extract the spatial radial features $\{W(v)\}_v$ and spatial autocorrelation features $\{E_l\}_l$
- Perform Cholesky decompositions of spatial autocorrelation matrices $\{E_l\}_l$.
- for $h = \{1, ..., H\}$ do
- Compute the initialization $\mathbf{w}_0(i)$ from the spatial radial features $\{W(v)\}_v$ and the *i*th reference projection \overline{S}_i .
- for $t = \{0, 1, \dots, T\}$ do
- 6: 5: Fix $w_t(i)$, and update $\{O_l(i)\}_l$ with respect to $w_t(i)$ via singular value decomposition.
- .7 Fix $\{O_l(i)\}_l$, and estimate $w_{l+1}(i)$ with respect to $\{O_l(i)\}_l$ via projected gradient descent.
- 9: $\dot{\infty}$ if $\frac{\|w_{t+1}(i)-w_{t}(i)\|_{2}}{\|w_{t}(i)\|_{2}} < \varsigma$, then
- end if Convergence is reached, set $w(i) = w_{t+1}(i)$, and break
- 11: 10: end for
- 12: Save the *i*th set of solutions $\{w(i), \{O_l(i)\}_l\}$
- end for
- Find the set of solutions that minimizes the MSE of autocorrelation features:

G.2)
$$\widetilde{i} = \arg\min_{i} \quad \sum_{l=0}^{\infty} \|P_{l}O_{l}(i) - B_{l}(w(i))\|_{2}^{2}$$

Return $\tilde{\boldsymbol{w}} = \boldsymbol{w}(i)$.

beneficial during reconstruction. determined by the lower-degree spherical harmonic expansion coefficients, which proves to be OMR-SC-F thus focuses more on recovering the low-resolution base structure of the density three degrees, which leads to a much stronger spherical harmonic frequency marching effect and the reductions of the gradient norms through the iterations are more significant in the first degrees, whereas the gradient norms of OMR-SC-F are much larger in the first three degrees, reductions of the gradient norms through the iterations are generally the same across different shown in Figure 12, the gradient norms of OMR-SC-S are more evenly distributed, and the This can be verified by comparing the gradient norms of OMR-SC-S and OMR-SC-F. As

noisy case turns out to be worse than the ab initio model. the ab initio models. In particular, due to the noisy features, the refinement of PTCH1 in the density map. Tables 10-12 show that the refinements are generally significantly better than relation coefficients of the ab initio models from OMR-SC-F by downsampling the projection Appendix H. Ab initio models from OMR-SC-F. We calculate the resolutions and cor-As discussed in section 6.2, a $33 \times 33 \times 33$ ab initio model is computed for every

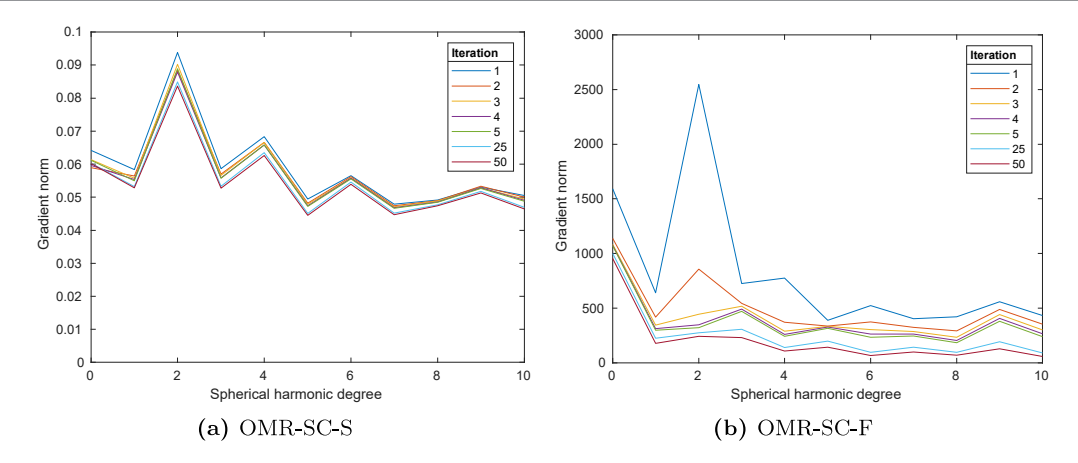


Figure 12. Gradient norms of OMR-SC-S and OMR-SC-F.

Table 10

Resolutions (in voxel) of the ab initio models and refinements produced by OMR-SC-F (FSC cutoff threshold=0.5).

	OMR-SC-F	D1	D2	D3	D4	D5	D6	D7	D8	D9	D10
Noiseless	Ab initio	20.88	30.77	11.83	12.21	15.29	13.70	32.36	13.97	14.20	13.76
	Refinement	6.70	9.62	5.90	7.28	$\bf 5.94$	4.10	10.63	7.48	8.46	5.54
Noisy	Ab initio	12.76	22.88	11.35	29.67	24.39	10.91	42.19	17.57	16.86	11.51
	Refinement	8.47	10.80	7.42	10.98	9.18	6.01	17.51	8.94	12.14	8.45

Table 11
Correlation coefficients of the ab initio models and refinements produced by OMR-SC-F.

	OMR-SC-F	D1	D2	D3	D4	D5	D6	D7	D8	D9	D10
Noiseless	Ab initio Refinement										
Noisy	Ab initio Refinement										

Table 12

Resolutions (Å) and correlation coefficients of the ab initio models and refinements produced by OMR-SC-F (FSC cutoff threshold = 0.5).

		F	Resolution	(Å)	Corr	elation co	efficient
	OMR-SC-F	CaS	НЈС	PTCH1	CaS	НЈС	PTCH1
Noiseless	Ab initio Refinement	25.77 14.04	45.21 29.38	27.08 16.52	0.87 0.93	0.69 0.78	0.80 0.86
Noisy	Ab initio Refinement	50.64 16.15	86.21 36.82	30.67 31.38	0.74 0.87	0.62 0.73	0.79 0.73

denoising the images as linear projection features Acknowledgment. We are grateful to Yifeng Fan for his help in providing the code for

REFERENCES

- [1] P. V. AFONINE, B. P. KLAHOLZ, N. W. MORIARTY, B. K. POON, O. V. SOBOLEV, T. C. TERWILLIGER, P. D. Adams, and A. Urzhumtsev, New tools for the analysis and validation of cryo-EM maps and $atomic\ models,$ Acta Crystallogr. Sect. D Struct. Biol., 74 (2018), pp. 814–840
- [2]ATKINSON AND W. HAN, Spherical Harmonics and Approximations on the Unit Sphere: An Introduc-Lecture Notes in Math. 2044, Springer, Cham, 2012.
- 3 Þ under group actions: BANDEIRA, B. BLUM-SMITH, J. KILEEL, Recovering orbits from invariants, Appl. Comput. Harmon. Anal., 66 A. Perry, J. Weed, and A. S. Wein,
- 4 Þ pp. 236–319. H. Barnett, Aliasing error of the $\exp(\beta\sqrt{1-z^2})$ kernel in the nonuniform fast Fourier transform. Appl. Comput. Harmon. Anal., 51 (2021), pp. 1–16. H. Barnett, J. Magland, and L. af Klinteberg,
- [5] \geq H. Barnett, H. Barnett, J. Magland, and L. af Klinteberg, A parallel nonuniform fast Fourier transform library based on an "exponential of semicircle" kernel, SIAM J. Sci. Comput., 41 (2019), pp. C479-
- [6] Bendory, A. Bartesaghi, and A. Singer, Single-particle cryo-electron microscopy: Mathematical theory, computational challenges, and opportunities, IEEE Signal Proc. Mag., 37 (2020), pp. 58-76.
- 7 Bendory, N. Boumal, W. Leeb, E. Levin, and A. Singer, Toward single particle reconstruction without particle picking: Breaking the detection limit, SIAM J. Imaging Sci., 16 (2023), pp. 886–910.
- ∞ Bepler, A. Morin, M. Rapp, J. Brasch, L. Shapiro, A. J. Noble, and B. Berger, Positive ods, 16 (2019), pp. 1153-1160. unlabeled convolutional neural networks for particle picking in cryo-electron micrographs, Nat. Meth-
- [9]Τ. BHAMRE, T. ZHANG, AND A. Proceedings of the 2015 IEEE 12th International Symposium on Biomedical Imaging, 2015, pp. 1048-SINGER, Orthogonal matrix retrieval in cryo-electron microscopy, in
- Bhamre, images, J. T. Zhang, and A. Singer, Denoising and covariance estimation of single particle cryo-EM Struct. Biol., 195 (2016), pp. 72 - 81.
- BHAMRE, T. Autocorrelation Analysis, preprint, arXiv:1704.07969, 2017. Zhang, and A. Singer, Anisotropic Twicing for Single Particle Reconstruction Using
- ۲. CHENG, N. croscopy, Cell, 161 (2015), pp. 438-Grigorieff, P. Penczek, and T. Walz, A primer to single-particle cryo-electron mi--449.
- A EM algorithm, J. R. Stat. Soc. Ser. B Stat. Methodol., 39 (1977), pp. 1-22. Dempster, Z . . .≍ Laird, and D. B. Rubin, Maximum likelihood from incomplete data via the
- Дисні, Learning, 2008, pp. 272–279. for learning in high dimensions, in Proceedings of the 25th International Conference on Machine S. Shalev-Shwartz, Y. Singer, and T. Chandra, Efficient projections onto the 11-bali
- [15]K Fan and Z. Zhao, Cryo-electron microscopy image denoising using multi-frequency vector diffusion in Proceedings of the 2021 IEEE International Conference on Image Processing, 2021, pp.
- [16]Ω H. Golub and J. H. Welsch, Calculation of Gauss quadrature rules, Math. Comp., 23 (1969), pp 221-233, s1-s10.
- [17] \mathbf{v} Gunasekar, B. E. Woodworth, S. Bhojanapalli, B. Neyshabur, and N. regularization in matrix factorization, in Advances in Neural Information Processing Systems 30, I. Guyon, U. V. Luxburg, S. Bengio, H. Wallach, R. Fergus, S. Vishwanathan, and R. Garnett, eds., Curran Associates, Red Hook, NY, 2017. Srebro, Implicit
- Ω HARAUZ AND M. HEEL, Exact filters for general geometry three dimensional reconstruction, Optik, 73 (1986), pp. 146–156.
- Þ Heimowitz, N. Sharon, and A. Jingel J. Imaging Sci., 14 (2021), pp. 689–716. N. Sharon, and A. Singer, Centering noisy images with application to cryo-EM, SIAM

- $\dot{\mathbf{v}}$ Huang and I. Dokmanić, Reconstructing point sets from distance distributions, IEEE Trans. Signal Process., 69 (2021), pp. 1811–1827.
- Ņ KAM, Determination of macromolecular structure in solution by spatial correlation of scattering fluctuations, Macromolecules, 10 (1977), pp. 927–934.
- Ņ KAM, The reconstruction of structure from electron micrographs of randomly oriented particles, J. Theoret. Biol., 82 (1980), pp. 15–39.
- Ņ Kam and I. Gafni, correlations, Ultramicroscopy, 17 (1985), pp. 251–262. Three-dimensional reconstruction of the shape of human wart virus using spatial
- Ę Biomedical Imaging, 2018, pp. 1569–1573. EM by autocorrelation analysis, in Proceedings of the 2018 IEEE 15th International Symposium on T. Bendory, N. Boumal, J. Kileel, AND A. SINGER, 3D ab initio modeling in cryo-
- Ŗ functions, Appl. Math. Comput., Mehrem, The plane wave expansion, infinite integrals and identities involving spherical Bessei 217 (2011), pp. 5360-5365.
- 26 27 \nearrow Messiah, Quantum Mechanics, North-Holland, Amsterdam, 1961.
- Park, et al., Natl. Acad. Sci. USA, 118 (2021), e2115849118. Symmetric activation and modulation of the human calcium-sensing receptor, Proc
- H F. PETTERSEN, T. D. GODDARD, C. C. HUANG, G. S. COUCH, D. M. GREENBLATT, E. C. MENG Comput. Chem., 25 (2004), pp. 1605–1612. AND T. E. FERRIN, UCSF Chimera-A visualization system for exploratory research and analysis, J.
- \mathbf{v} H. Scheres, A Bayesian view on cryo-EM structure determination, J. Mol. Biol., 415 (2012), pp 406 - 418.
- $\dot{\mathbf{v}}$ H. Scheres, Relion: Implementation of a Bayesian approach to cryo-EM structure determination, J.
- [31] P. H. (1966), pp. 1–10. Struct. Biol., 180 (2012), pp. 519-530. Schönemann, A generalized solution of the orthogonal Procrustes problem, Psychometrika, 31
- N. SHARON, J. KILEEL, Y. KHOO, B. LANDA, AND A. SINGER, Method of moments for 3D single particle ab initio modeling with non-uniform distribution of viewing angles, Inverse Problems, 36
- Ħ Sigworth, (1998), pp. 328-339. A maximum-likelihood approach to single-particle image refinement, J. Struct. Biol., 122
- \triangleright SINGER, Mathematics for cryo-electron microscopy, in Proceedings of the International Congress of Mathematicians, 2018, pp. 3995-4014.
- \triangleright SINGER, Wilson statistics: Acta Crystallogr. Sect. A, 77 (2021), pp. 472-Derivation, generalization and applications to electron cryomicroscopy -479.
- \triangleright SINGER AND Y age, version 0.14, 2018, Shkolnisky, http://spr.math.princeton.edu, Algorithms for Single Particle Reconstruction, ASPIRE software pack-
- Ω M. Spahn, E. Jan, RNA-based translation factor, Cell, 118 (2004), pp. 465-475. ization of a viral internal ribosome entry site bound to human ribosomes: A. Mulder, R. A. Grassucci, P. Sarnow, and J. Frank, Cryo-EM visual The IRES functions
- Ω quadrature-weights-and-nodes. VON WINCKEL, 2004,Legendre-Gauss Quadrature Weights and Nodes, https://www.mathworks.com/matlabcentral/fileexchange/4540-legendre-gauss-MATLAB Central File
- Ξ. Wagner, F. Merino, M. Stabrin, T. Moriya, C. Antoni, A. Apelbaum, P. Hagel, O. Sitsel fully automated particle picker for cryo-EM, Commun. Biol., 2 (2019), 218. R. SHAIKH, P. LILL, C. GATSOGIANNIS, AND S. RAUNSER, SPHIRE-crYOLO is a fast and accurate T. Raisch, D. Prumbaum, D. Quentin, D. Roderer, S. TACKE, B. SIEBOLDS, E. SCHUBERT, T.
- WANG, H. GONG, G. LIU, M. LI, C. YAN, T. XIA, X. LI, AND J. ZENG, Deeppicker: A deep learning approach for fully automated particle picking in cryo-EM, J. Struct. Biol., 195 (2016), pp. 325-336
- M Zehni, S. Huang, I. Dokmanić, tomography,2019, pp. 5027-5031. in Proceedings of the IEEE International Conference on Acoustics, Speech, and Signal AND Z. Zhao, Geometric invariants for sparse unknown view
- ZEHNI, S. HUANG, I. DOKMANIĆ, AND Z. in Proceedings of the IEEE Internation International Conference on Acoustics, Speech, and Signal ${
 m ZHAO},\,3D$ unknown view tomography via rotation invariants

- [43] Z. Zhao, Y. Shkolnisky, and A. Singer, Fast steerable principal component analysis, IEEE Trans. Comput. Imaging, 2 (2016), pp. 1–12.
 Zhao and A. Singer, Fourier-Bessel rotational invariant eigenimages, J. Opt. Soc. Amer. A, 30 (2012)
- [44] Z. (2013), pp. 871–877.
- [45]Y. Zhu, Q. Ouyang, and Y. Mao, A deep convolutional neural network approach to single-particle recognition in cryo-electron microscopy, BMC Bioinform., 18 (2017), pp. 1–10.